Characterisation and Assessment of a Broadband Tunable Ti:Sapphire Laser for use in C.A.R.S. Spectroscopy

By
J.A. Anderson

Submitted in partial fulfilment of the requirements
for the degree of Master of Physics
in the
Department of Physics, University of Cape Town

June 10, 1996 Supervisor: Prof. H.S.T. Driver

Contents

Chapter 1

Introduction

1.1 Historical Background

In 1963, Bell Labs researchers reported the first vibronic laser, a nickel-doped magnesium fluoride device [1]. The vibronic laser has a transition where the photon emission is coupled to vibrational phonon emission into the crystal. Thus, although the total energy of the transition is fixed, there is a continuous partition of the energy into these two forms allowing a broad range of possible photon energies. This laser and similar ones which followed had the serious drawback of needing to be at cryogenic temperatures in order to operate. In 1977, however, alexandrite was made to lase at room temperature [2]. This led to the investigation of many divalent and trivalent transition-metal doped crystals. Most, however, suffered from excited state absorption which led to reduced gain.

The Ti:Sapphire laser ($Ti : Al_2O_3$) laser was first suggested in 1982 by Moulton [3] as a source of broadband tunable laser radiation. The crystal does not show appreciable excited state absorption, so almost the entire vibronic emission range is available for lasing. The fluorescence allows continuous tuning over the range 660 to 970 nm. The

first observed lasing from $Ti : Al_2O_3$ was obtained using a coaxial flashlamp-pumped Coumarin 504 dye laser pump [3]. Since then room temperature cw laser operation with an output power of 1.6 W [4]; self-injection locked line-narrowed Q-switched operation with 1 pm bandwidth [5]; single frequency, tunable cw operation [6]; pulsed operation with output of 2 J [7] have been produced.

The most common systems are at present the frequency doubled Nd:YAG pump for pulsed operation and the Argon-Ion pump for continuous-wave operation [3][8][9]. Both systems are commercially available as either ready made systems or in kit form.

1.2 Motivation

The University of Cape Town (UCT) Laser Group has been involved in extensive research in the field of Coherent Anti-Stokes Raman Spectroscopy (CARS). This is a widely used non-linear spectroscopic technique which allows the measurement of species concentrations and temperatures with good spatial and temporal resolution. This capability has led to much fruitful work in the field of turbulent combustion analysis and more specifically by UCT, nitrogen gas thermometry of methanol burning engines.

Our system employs a frequency doubled, single longitudinal mode Nd:YAG laser as the pump and a broadband dye laser as the Stokes beam. Information regarding species concentrations and temperatures is obtained through analysis of the pulse shape of the induced CARS emission. The accuracy of the information is therefore limited by any spectral fluctuations of the CARS signal. Both at UCT and elsewhere large shot-to-shot fluctuations have been observed [10][11][12] and there is general agreement that the major source of this noise is the stability of the Stokes laser [13].

It is believed that spectral fluctuations in the Stokes laser originate in the statistical nature of the quantum noise leading to laser buildup [14][15]. Early studies assumed

the modes of the laser to be uncorrelated and statistically independent [16]. More recent work has shown that noise is largely due to mode competition effects. Since different modes rely on the same upper state population, the first longitudinal mode to build up enough spontaneous emission to rise above threshold, will reduce the available gain for other modes. The particular modes which achieve this will vary from shot to shot, causing spectral fluctuations. Modeless lasers have been used as the Stokes beam in order to reduce these mode competition effects [17] [18]. Since in our present system the Stokes laser consists of a liquid dye laser with unavoidable flow complexities, it seems reasonable to propose that a solid-state laser would have better shot-to-shot reproducibility. The Ti:Sapphire laser was therefore chosen as a possible substitute for the dye Stokes laser. With a 532 nm pump beam one requires a Stokes beam at 607 nm in order to perform CARS. Since the red $Ti : Al_2O_3$ fluorescence peaks at $\sim$ 800 nm as compared to the 607 nm dye Stokes pulse, one needs to shift the pump beam to longer wavelengths than 532 nm. This pump can be provided by Stimulated Raman Scattering (SRS) in H_2 [19]. The Ti:Sapphire laser is then required to provide the Stokes beam at 812 nm.

1.3 Research Overview

This thesis deals specifically with the operation of the Ti:Sapphire laser. The laser was obtained from BMI Industries in a kit form. The component parameters were first determined to use in theoretical models of the laser's operation. The laser was then assembled and optimized in order to get the most efficient output. Runs of shots were recorded at various tuned wavelengths and energies.

This allowed accurate comparisons with the models and assessment of the praticability of use of the laser as the Stokes beam in a CARS system. The shot-to-shot noise was also measured and an attempt made to identify the major sources of this noise. Finally a comparison of the noise values for the Ti:Sapphire laser was made with the values for the dye laser presently used in CARS.

Chapter 2

Experimental Setup

2.1 Nd:YAG Laser

The Nd:YAG laser provides the pump energy for the Ti:Sapphire laser. The Nd:YAG is a pulsed solid state laser operating on a single longitudinal mode. The oscillator consists of a flashlamp pumped Nd:YAG rod in a cavity with passive Q-switching by means of a saturable absorbing dye. This produces an infrared beam at 1064 nm with a pulse length of approximately 30 ns (depending upon the concentration of the saturable dye). This beam is then amplified in two flashlamp pumped amplifiers. Finally the beam passes through a KDP doubling crystal which doubles the frequency to 532 nm in the green region of the visible spectrum. This provides a beam with a gaussian profile with a diameter of 4 mm and length of 20 ns. The polarisation of the beam can be adjusted. For all but one set of data, the beam was polarised horizontally.

The energy of the pump beam can be continuously tuned by changing the applied voltage on the flashlamp pumps. The green pump energy passes through various components between leaving the Nd:YAG laser and reaching the $Ti : Al_2O_3$ crystal

(including four right-angled prisms for beam alignment). For calibration purposes, therefore, measurements were made at both positions. The energy was determined using a Scientech calorimeter with the laser firing at 1 Hz repetition rate (the rate used throughout all experiments).

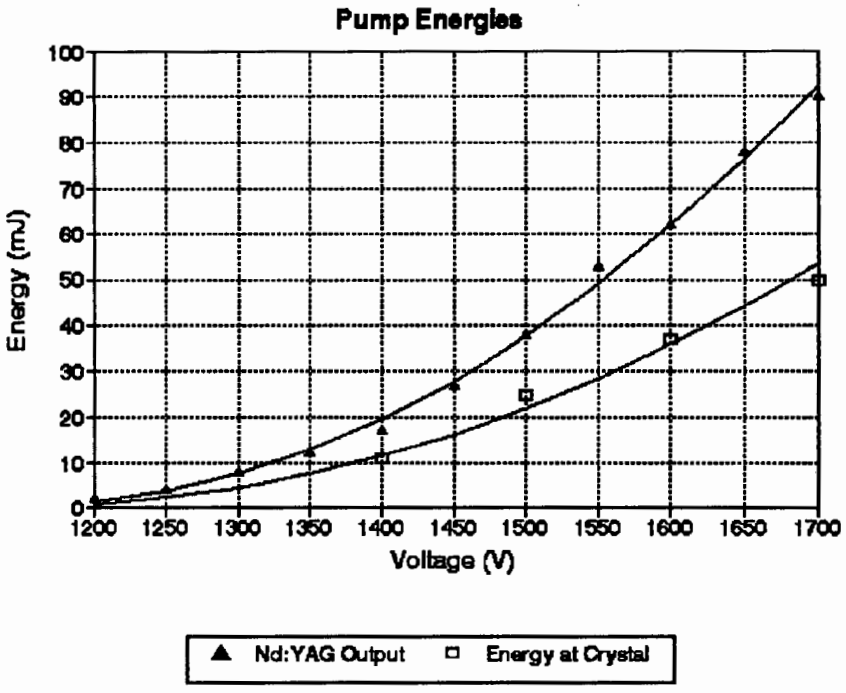

Figure 1: Nd:YAG Pump Beam Energy

The results in figure 1 show a parabolic least squares fit to the observed energy data at the exit of the Nd:YAG laser. The fit to the data at the crystal is simply a least squares fit of the same parabolic curve as that for the exit position energies, multiplied by a transmission factor. The fit produced a reduction of the green pump energy between exiting the Nd:YAG laser and reaching the crystal of 58%, which means this factor is significant when considering the actual energy available for pumping the $Ti : Al_2O_3$ crystal.

2.2 Ti:Sapphire Laser

In this section each component of the Ti:Sapphire laser will be discussed in the order in which the green pump beam would encounter it.

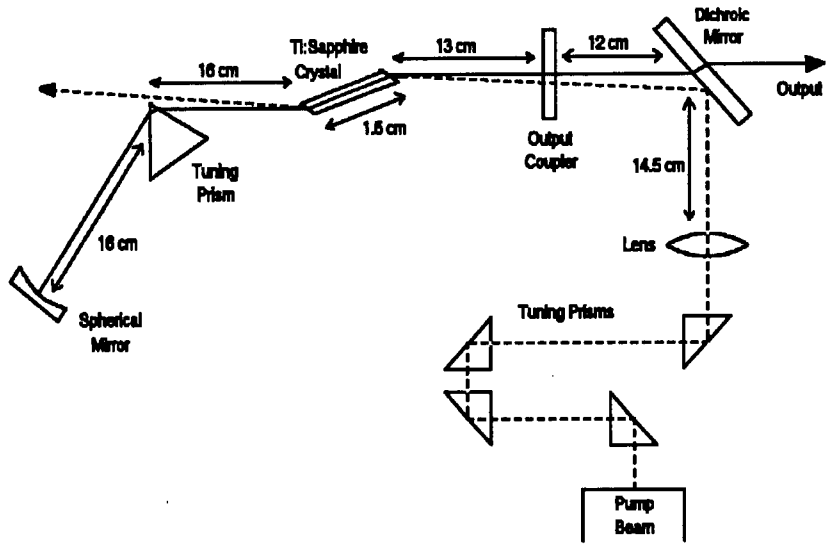

Figure 2: Component Layout of the Ti:Sapphire laser

2.2.1 Prisms,Lens,Dichroic Mirror

When the Ti:Sapphire laser was assembled for the first time it was discovered that adjustment of the tilt of the dichroic mirror was not sufficient to ensure optimal entry of the green pump into the crystal. This led to considerable frustration when trying to optimize the Ti:Sapphire laser output. We therefore decided to introduce four right-angled prisms into the green beam with both lateral movement and tilt available on the prism closest to the dichroic mirror. This allowed us to adjust both the position and direction of the pump beam.

Adjustment of the lens (which has focal length 58±1 cm) allows the area of the pump beam at the crystal to be changed. This is important as one wants sufficient pump intensity to get the Ti:Sapphire laser above threshold, while not concentrating the beam to such an extent that it burns the crystal.

As noted earlier the dichroic mirror was left in one position and not used to optimize the pump beam direction. It still, however, acted to reflect the green pump into the cavity while allowing the red ouput to pass through and be examined free from interference from the green.

2.2.2 Output Coupler

The output coupler reflectance was determined using a Tungsten filament source, Heath monochromator and photomultiplier which is sensitive over the range 350-850 nm. Measurements for beams propagating both into and out of the cavity were taken. The reflectance of the output coupler for a particular lasing wavelength is important for determining the cavity decay lifetime for models of the laser's operation.

The first point to note in figure 3 is that the reflectance for beams escaping from the cavity is an almost constant R $\approx$ 0.6 over the tunable range of $Ti : Al_2O_3$, viz. 650-1000 nm. The drop off at long wavelengths above 850 nm is more likely due to drop off in photomultiplier response than a true drop off in reflectivity.

Other features which are of interest are the peaks in the range 300-500 nm due to the coatings on the surface of the glass. The wavelength of 532 nm, corresponding to the frequency doubled Nd:YAG pump beam, shows a distinct drop in reflectance for beams entering the cavity (figure 4). This ensures that as much of the pump beam as possible gets through to the $Ti : Al_2O_3$ crystal.

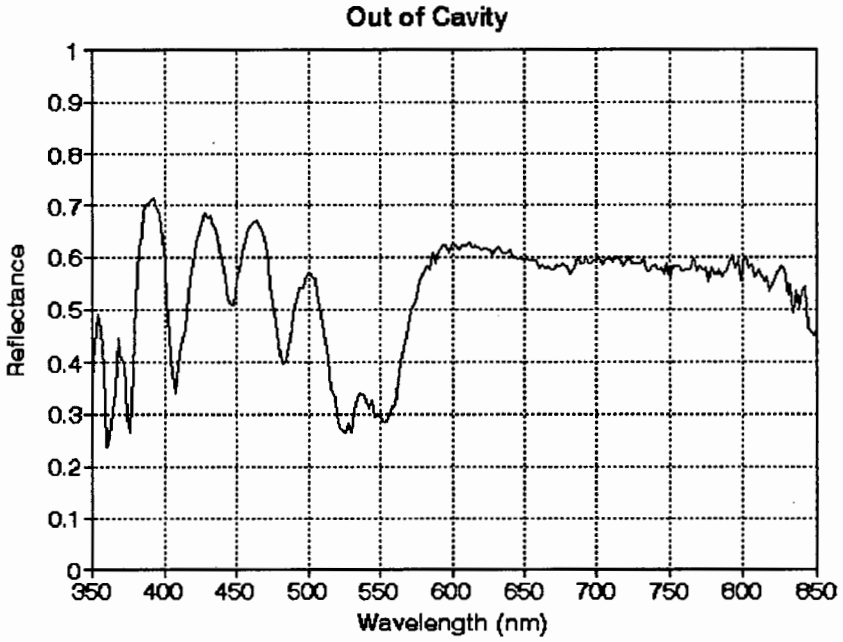

Figure 3: Output Coupler Reflectance Spectrum Inside Cavity Face

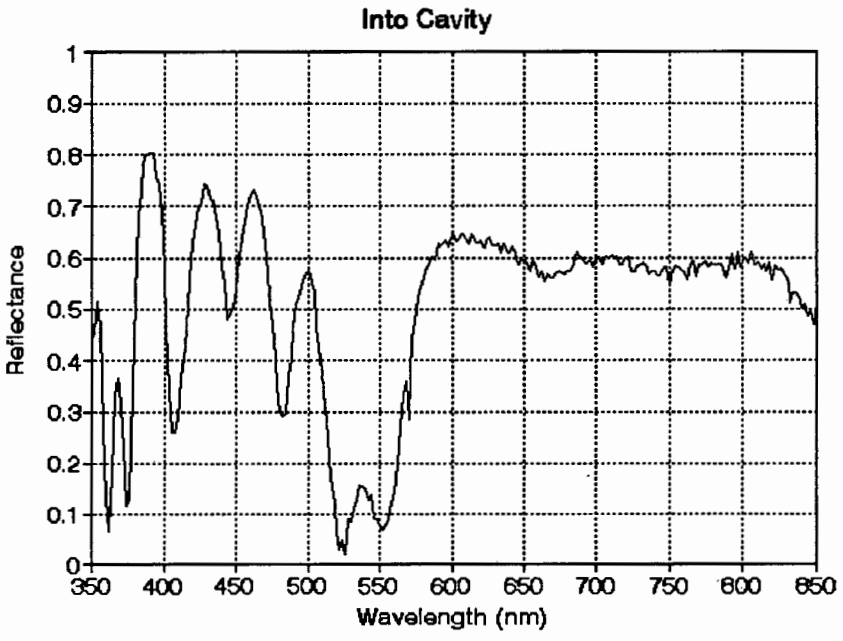

Figure 4: Output Coupler Reflectance Spectrum Outside Cavity Face

2.2.3 Ti:Sapphire Crystal

The $Ti : Al_2O_3$ crystal is the next component to be encountered. The crystal was grown by Union Carbide Corporation using the Czochralski method. It has a cross-section of 3 mm $\times$ 3 mm and a length of 15 mm. The ends are polished at the Brewster angle of 60.5 degrees. The entrance and exit ends are flat to 0.1 λ and the long sides are ground. It also has a FOM of more than 300 (this is the ratio of absorption cross sections at 532 nm and 800 nm).

An important parameter needed in modelling is the number density of the absorbing and emitting atoms. This is determined by the doping concentration of the crystal. Sapphire (Al_2O_3) has a density of 3.965 $\times$ 10^3kg/m^3[20] and an atomic weight of 102g/mol. This gives a number density of Sapphire "molecules" ($N(Al_2O_3)$) of 2.3 $\times$ 10^{28}/m^3, with atomic weigths of 144 and 102 for $Ti : Al_2O_3$ and Al_2O_3 respectively. Our crystal is quoted as 0.15% Titane, which gives the following equation:

$$\frac{0.15}{100} = \frac{N(Ti_2O_3)}{N(Al_2O_3)} \times \frac{144}{102} \tag{1}$$

This gives a number density of Titane ($N(Ti_2O_3)$) of 2.44 $\times$ 10^{25}/m^3 and a number density of Titanium ($N(Ti^{3+})$) of 4.9 $\times$ 10^{25}/m^3 for 0.15% Ti_2O_3 in Al_2O_3. The crystal used by Moulton [3] has a similar concentration.

The other important characteristics of the crystal are its absorption and emission spectra.

From figure 5 we can see that the $Ti : Al_2O_3$ absorption cross sections for the π and σ polarisations are 5.0 $\times$ 10^{-20} cm^2 and 2.2 $\times$ 10^{-20} cm^2 respectively at the pump wavelength of 532 nm. The $Ti : Al_2O_3$ π polarised fluorescence curve can be approximated by a Poisson distribution [9] as follows :

$$\sigma_f = \sigma_s \frac{m^p}{p!} = \textit{Cross section for emission} \tag{2}$$

where

$\sigma_s = 1.663 \times 10^{-25}$ m^2 = Normalisation factor
$m = 7.074$ = Expectation value of phonons emitted
$p = \frac{\nu_0 - \nu}{\nu_s}$
ν = variable = Lasing frequency
$\nu_0 = 4.853 \times 10^{14}$ Hz = Energy of zero phonon line at 626 nm
$\nu_s = 1.630 \times 10^{13}$ Hz = Average phonon energy

2.2.4 Tuning Prism, Spherical Mirror

The BMI prism which we are using is made of SF2 glass. The refractive index is listed in the Spindler and Hoyer Catalogue with λ in μm as follows:

$$n^2 = 1 + \frac{1.403\lambda^2}{\lambda^2 - 0.01058} + \frac{0.2318\lambda^2}{\lambda^2 - 0.04932} + \frac{0.9391\lambda^2}{\lambda^2 - 112.4} \tag{3}$$

The values derived from equation 3 are necessary for modelling the wavelength dependence of the Ti:Sapphire laser spectra.

Finally the rear spherical mirror completes the resonant cavity. The mirror is coated so that the reflectance for all relevant lasing frequencies is R $\approx$ 1. The radius of curvature of the mirror was measured as 106$\pm$1 cm.

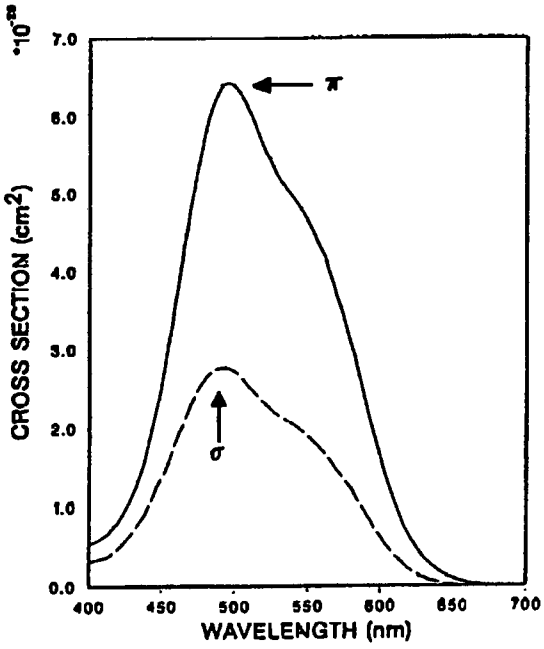

Figure 5: Absorption cross section obtained by Moulton

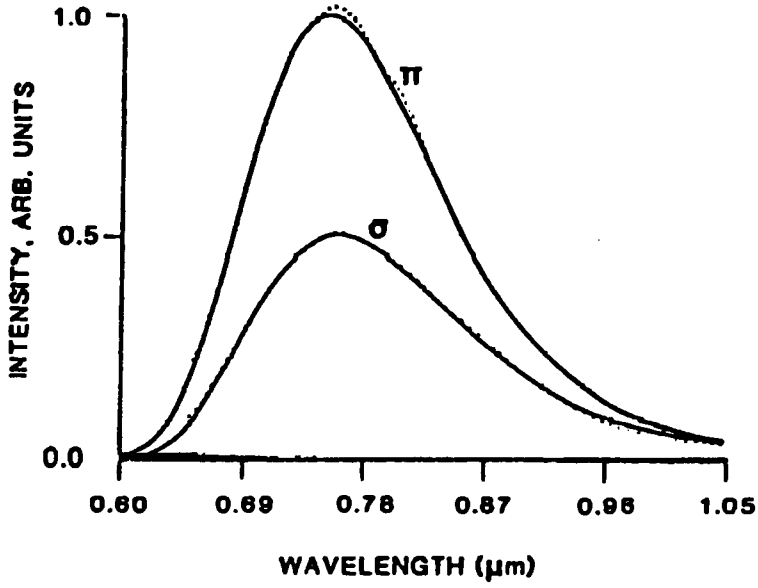

Figure 6: Emission cross section obtained by Eggleston et al.

2.2.5 Laser Alignment

All the components listed in the previous section were placed on, and attached to, an optical table consisting of a 500 × 600 × 12 mm sheet of steel in order to assure mechanical stability. A HeNe laser was mounted rigidly at the dichroic mirror end of the table.

The HeNe laser operating at 632.8 nm was directed into the cavity through the dichroic mirror, parallel to the table and normal to the output coupler along the path of the expected red Ti:Sapphire laser output. The crystal was then placed in the HeNe beam in such a way as to ensure central propagation of the beam down the crystal. The mounting of the crystal was equipped with micrometer movements in order to adjust both the height and the position accurately. The prism was then placed in the light path so that it just intercepted the beam at the corner around which it could rotate. The prism was then rotated using the micrometer screw on the mounting until the HeNe beam was at minimum deviation. The spherical mirror was then introduced and angled so as to reflect the beam back upon itself. Fine adjustment of the angles of the output coupler and spherical mirror were then performed in order to align the resonant cavity. Confirmation of the accuracy of this process was obtained from the interference effects observed in the crystal. The scattered light from the crystal was observed to get brighter and dimmer with any small vibration of the optical table. The prism was then rotated to an angle corresponding to an ouput wavelength within the emission cross section of the $Ti : Al_2O_3$ crystal while still being visible to the naked eye ($\sim$ 750nm).

The Nd:YAG pump beam was then fed into the cavity off the dichroic mirror. The angle of the mirror was adjusted in order to ensure that the green beam entered the crystal. A set of runs of shots was then taken. Subsequent analysis of the data, however, showed that the Ti:Sapphire laser was not working as efficiently as possible. Since the cavity appeared to be well aligned, the blame was placed on the direction of the green pump. In order to align the pump more accurately four right angled prisms

were placed in the path. The green beam was then aligned so that it fell centrally on the front face of the crystal, while missing the tuning prism as closely as possible. This completed the exact alignment of the laser.

2.3 Detectors

2.3.1 Spectrometer

The red Ti:Sapphire laser output is led to the spectrometer by a set of adjustable mirrors in order to ensure accurate alignment with the entrance slit. The red beam expands from the slit and falls on a concave holographic grating with 2100 grooves per mm. The diffracted beam then falls onto a focusing telescope and then onto the detector. The PARC EG&G 1421 Optical Multichannel Analyser (OMA) detector consists of a 1024 pixel array controlled by a PARC 1461 Detector Interface. The system is capable of recording all the spectra in a typical 30 shot run at a 1 Hz repetition rate.

As the gearing controlling the rotation of the grating has a limited travel, it was found to be necessary to rotate the grating manually and then to recalibrate the wavelength scale read-out so that longer wavelengths could be analysed. This was achieved by using the grating equation for 1st order spectra:

$$\lambda = d\sin(\alpha + D/2)\cos(D/2) \tag{4}$$

$$\alpha = \arcsin\frac{\lambda}{2d\cos(D/2)} - D/2 \tag{5}$$

where

λ = wavelength

$d = 476$ nm = groove seperation

α = angle between incident beam and grating normal

$D = 5$ degrees = angle between entrance slit and detector

Knowing the calibration wavelength λ (532 nm for Nd:YAG, say) one can calculate the grating angle α (31.5 degrees) using equation 5. If the grating is then loosened and rotated so that λ is observed at a lower scale reading (338 nm, say), the amount by which the grating has been manually rotated (13.2 degrees) can be calculated from equation 5 by noting the angle implied by the new scale reading (18.3 degrees) from equation 4. For any other scale readings one can then calculate the angle without the manual rotation from equation 4, add the extra manual rotation and calculate the actual wavelength from equation 5

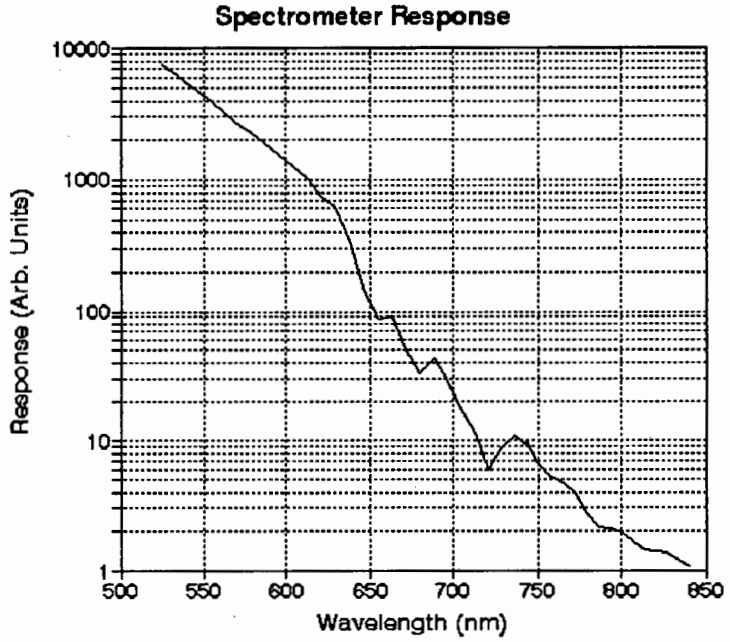

Figure 7: Spectrometer Response Spectrum

Noting that the spectrometer was not built for longer wavelengths (> 700 nm),

an investigation of the spectrometer response function was deemed necessary. A Tungsten filament source was used and spectra at 10 nm wavelengths intervals were taken. All pixels for a particular spectrum were added to give a relative measure of the observed energy.

The most important feature of figure 7 is the very strong drop in sensitivity at wavelengths approaching 800 nm. This effectively limited any spectral data to wavelengths below 800 nm. Another interesting feature is the appearance of anomalous peaks in the response. These were confirmed by repeated measurements of selected regions of the spectrum. These features make any inference of relative Ti:Sapphire laser output energy from the spectrum rather difficult.

2.3.2 Oscilloscope and CCD Camera

The temporal profile of the Ti:Sapphire laser was obtained using an oscilloscope-CCD camera combination. A small sample of the green pump beam was fed to a PIN photodiode (Sopra) through an optic fibre. A beam splitter in the path of the red output diverted a portion of the beam away from the spectrometer so that it fell directly onto the diode. The intensity of this beam was controlled by the insertion of neutral density filters in the beam path to the diode. This ensured that the PIN diode operated within its known linear response range and avoided the possibility of detector saturation. The green beam was thus delayed relative to the red output during its path through the several metres of optic fibre. The magnitude of this delay was determined to be 16.8 ns by allowing the green to follow the same path as the red output, and then comparing it with the green passing through the optic fibre.

The signal from the diode was then displayed on an oscilloscope (Tektronix 2467 350 MHz). The osilloscope was triggered by the green pump beam. The oscilloscope screen was then imaged using a 512 $\times$ 512 pixel CCD camera (PULNiX TM-6EX).

The camera was controlled by a computer with a frame grabber card (Imaging Technology OFG) connected to an image archiving system (Datacell SCVI-3) which saved the images to a SCSI hard drive. This allowed images to be saved at the pump repetition rate of 1 Hz. As the images were taken they could be viewed on a RGB monitor. This method of recording temporal data was used for the first time. It was a major improvement over the older method of photographing the oscilloscope screen, as it provided a digitised signal from the fast analogue oscilloscope which facilitated accurate temporal analysis of the trace.

A calibration image of the oscilloscope could be taken and the trace images superimposed on this. Analysing the trace image gave an array of 512 intensity values (height of the trace from the bottom of the image) across the pixel array. The calibration image was used to determine the time span represented by one pixel by counting the number of pixels in one division of the oscilloscope scale.

2.3.3 Energy Measurements

Relative changes in input and output pulse energies could be obtained for each run by integrating the area under the oscilloscope trace to give a trace energy in arbitrary units. The green input trace energy could then be calibrated by fitting the measured average pump energy at the crystal (obtained using a calorimeter (Scientech) connected to a multimeter (Fluke 75)) at a particular voltage setting to the average trace energy at that voltage. Calibration of the red output trace energy was performed in a similar manner. The red output could, unfortunately, only be calibrated for the final run, as the measurement required the dismantling of the train of mirrors directing the beam to the spectrometer. This calibration could not be extended to other runs as the exact response function of the PIN photodiode was not known.

Chapter 3

Preliminary Calculations

3.1 Tuning Angle

In order to select a particular wavelength at which the laser should lase, one has to angle the prism so that the desired wavelength, after passing through the prism, is reflected by the rear cavity mirror colinearly back to the same point on the prism. In order to achieve this, one needs to know which angle of the prism corresponds to which wavelength.

From equation 3 we can calculate the refractive index n for a particular wavelength. The deviation angle D of a beam for a prism of corner angle A (our prism has $A =$ 60 degrees) is then given by:

$$D = \theta_i + \arcsin[n \times \sin\{A - \arcsin(\frac{\sin\theta_i}{n})\}] - A \tag{6}$$

Figure 8 shows the results obtained from equation 6. If we arrange the cavity so that with a 632 nm HeNe beam at its angle of minimum deviation ($\sim$ 50.5 degrees) we

have resonance (or at least interference), then we need to turn the prism through an angle of between 3.0 degrees and 7.5 degrees to get wavelengths between 685 and 900 nm respectively to follow the same path as the HeNe beam, thereby causing these wavelengths to resonate.

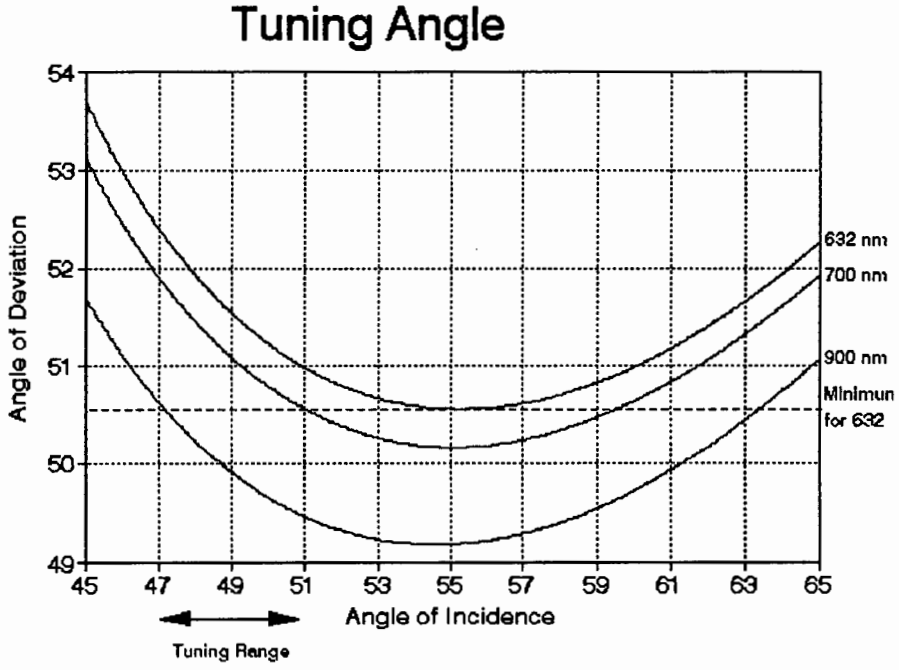

Figure 8: Deviation curves for the SF2 prism

3.2 Laser Resonator

As noted earlier the cavity of the Ti:Sapphire laser contains a prism for wavelength selection. Considerable work has been done with reference to prisms in dye laser cavities by Duarte and others [21]. The later section dealing with the modelling of the spectral output investigates these properties in more detail. In order to investigate the properties of a single cavity mode once the prism has been tuned to a particular wavelength, however, the prism may be ignored and the cavity assumed to be linear. This greatly simplifies the analysis, while still producing vital information regarding

mode volumes and stability.

The resonator is quasihemispherical with the plane mirror situated 44 cm from the spherical mirror with radius of curvature of 106 cm. Considering the formulae derived by Kogelnik and Li for a gaussian beam in a resonant cavity the spot sizes (beam radii) w_1 and w_2 at the mirrors with radii of curvature R_1 and R_2 and separation L are in general given by [22]

$$w_1^4 = (\frac{\lambda R_1}{\pi})^2 \frac{R_2 - L}{R_1 - L} \frac{L}{R_1 + R_2 - L}$$
$$w_2^4 = (\frac{\lambda R_2}{\pi})^2 \frac{R_1 - L}{R_2 - L} \frac{L}{R_2 + R_1 - L} \tag{7}$$

The equations 7 can now be simplified by noting that one mirror has $R_1 = \infty$

$$w_1^2 = (\frac{\lambda}{\pi})[L(R_2 - L)]^{\frac{1}{2}}$$
$$w_2^2 = (\frac{\lambda}{\pi})R_2(\frac{L}{R_2 - L})^{\frac{1}{2}} \tag{8}$$

These give the result that for a wavelength of 800 nm the spot on the plane mirror has a radius of 0.36 mm. This is also the beam waist size w_0. The spot on the spherical mirror has a radius of 0.47 mm. The spot size a distance z away from the beam waist is given by

$$w(z) = w_0(1 + \frac{z^2}{z_0^2})^{\frac{1}{2}} \qquad with \qquad z_0 = \frac{\pi w_0^2}{\lambda} \tag{9}$$

This gives the spot size at the crystal as 0.38 mm. This means that a very small volume of the crystal is actually used for gain. The volume of the crystal is 135 mm^3 and the volume of the TEM$_{00}$ mode in the crystal only 6.8 mm^3, representing a use of only some 5% of the available $Ti : Al_2O_3$. The very narrow cavity mode is therefore not ideal for getting the most out of the $Ti : Al_2O_3$ crystal.

3.3 Self Focus

Preliminary work on the Ti:Sapphire laser by other students in the UCT Physics Department indicated a tendency for the surfaces of the crystal to become pitted by the green pump beam. In fact this problem became so pronounced that the original BMI crystal had to be replaced. It therefore appeared important to gain a feel for the damage thresholds involved with the Ti:Sapphire laser.

Self focusing of an optical beam occurs due to the focusing effect of the nonlinear refractive index of a medium overcoming the spreading of the beam by diffraction. This suggests a simple way of working out the beam power at which this phenomenon will be observed. When the focusing effect exactly balances the divergence effect the beam will be trapped and not change its diameter. The beam power at which this occurs is termed the critical power [23].

We consider a circular optical beam of diameter D and uniform intensity in a material with a refractive index which can be expanded in terms of the electric field strength (in esu) as

$$n = n_0 + n_2 E^2 + ... \tag{10}$$

The beam would be expected to expand due to diffraction with an angular divergence of

$$\theta_d \approx \frac{1.22\lambda_0}{n_0 D} \tag{11}$$

Assuming that the beam is diverging at this angle, then in order to stop it expanding the beam must be refracted back at the critical angle for total internal reflection

$$\sin(90^o - \theta_d)(n_0 + n_2E^2) = sin(90^o)(n_0)$$

$$\cos\theta_d = \frac{1}{1 + \frac{n_2E^2}{n_0}}$$

$$\theta_d \approx (\frac{2n_2E^2}{n_0})^{\frac{1}{2}} \tag{12}$$

Now setting this equal to our previous expression for θ_d

$$\frac{1.22\lambda_0}{n_0D} = (\frac{2n_2E^2}{n_0})^{\frac{1}{2}}$$

$$E^2 = \frac{(1.22\lambda_0)^2}{2n_2}\frac{1}{D^2n_0} \tag{13}$$

And noting that

$$P = \frac{\pi D^2}{4}I = \frac{\pi D^2}{4}(\frac{c}{8\pi})n_0E^2 \tag{14}$$

We get a critical power of

$$P_c = \frac{(1.22\lambda_0)^2c}{64n_2} \tag{15}$$

This is, however, only a crude approximation as it does not take into account the gaussian nature of the beam. A more accurate, but rather more lengthy treatment which has been checked both theoretically [24] [25] and numerically [26] gives the critical power for gaussian beams as

$$P_c = \frac{{\lambda_0}^2c}{32\pi^2n_2} \tag{16}$$

It is noted by Chaio et al. [23] that the predominant mechanism for the refractive index change in Sapphire is electrostriction (the distortion by an applied field of the atomic electron clouds). A value of 0.2×10^{13} esu is quoted for the nonlinear refractive index n_2. This gives a value of 1.4 MW for the critical power. Assuming the green pump beam has a gaussian temporal profile with FWHM of 20 ns, this implies a pump energy of some 30 mJ. This is well within the capabilties of our Nd:YAG laser, so there is a very real danger of damage to the crystal, and the fact that damage has already occurred is not surprising.

Surface damage can occur without self focusing. W.Rapoport et al. [27] report a surface damage threshold of 4 - 5 Jcm^{-2}. Naturally factors such as the quality of the polished finish and dust contamination can alter this value, however it is still a useful order of magnitude estimate. In our experiments a maximum pump energy of 52 mJ was used, focused down to an area of 13×10^{-6} m^2. This corresponds to an irradiance of 0.4 Jcm^{-2} - an order of magnitude below the quoted threshold. More worrying, however, is the possibilty that "hot" spots may appear in the green pump, particularly on those occasions when the Nd:YAG produces a multimode shot, and burn the crystal in just a small area. If our 52 mJ of pump were to be focussed onto an area 1 mm square, the irradiance would be 5.2 Jcm^{-2} which is of the order of the threshold for surface damage. The surface of the crystal was thus watched carefully during the experiments, but no additional damage was seen to occur.

Chapter 4

Modelling

4.1 Temporal Model

4.1.1 Rate Equations

The energy level structure of Ti^{3+} can be modelled as a 4 level system [9] (see figure 9).

The pump takes the atom from an initial ground state S_0 to a short lived excited state S_3. The electron then rapidly falls to a band of states S_2. This is a metastable state with a lifetime assumed much longer than that of the state S_3. Transition from state S_2 to S_1 produces the lasing frequency. A rapid transition then occurs back to the ground state. We thus see that the transition lifetimes have the properties:

$$\tau_{32} \ll \tau_{21} \qquad \tau_{10} \ll \tau_{21} \tag{17}$$

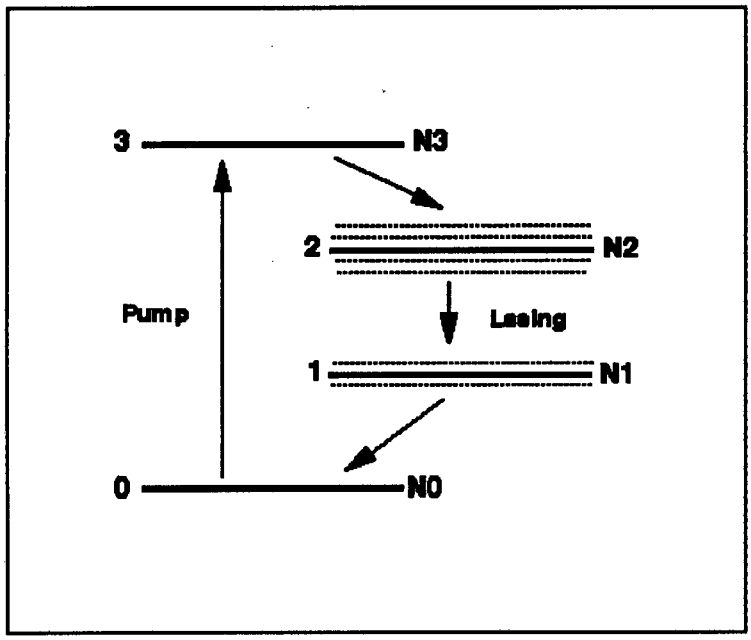

Figure 9: Energy Level Diagram showing Transitions

The number densities N in the various states S with the initial ground state population N_{00} are:

$$N_3 + N_1 \ll N_2 \qquad\qquad N_0 = N_{00} - N_2 \tag{18}$$

These assumptions lead to the coupled rate equations for N_2, the population density in the upper state, and n the number of photons in the cavity [28].

$$\frac{dN_2}{dt} = \underbrace{\frac{I_p}{h\nu_p}\sigma_p N_0}_{pump} - \underbrace{\frac{nc}{V}\sigma_f N_2}_{stimulated\ emission} - \underbrace{\frac{N_2}{\tau_{21}}}_{spontaneous\ emission} \tag{19}$$

$$\frac{dn}{dt} = \underbrace{-\frac{n}{t_c}}_{cavity\ decay} + \underbrace{\frac{nc}{V}a_r l\sigma_f N_2}_{stimulated\ emission} + \underbrace{\frac{1c}{V}a_r l\sigma_f N_2}_{spontaneous\ emission} \tag{20}$$

Where the physical constants are:

$c = 3 \times 10^8 \text{ms}^{-1}$ = Speed of light
$h = 6.63 \times 10^{-34} \text{Js}$ = Planck's constant

Cavity parameters are:

$a_r = 5 \times 10^{-7} \text{m}^2$ = Mode area
$L = 0.44\text{m}$ = Mode length
$V = a_r L$ = Mode volume
$\tau_c = \frac{2L}{c \ln(\frac{1}{R_1 R_2})} = 5.7 \times 10^{-9}\text{s}$ = Cavity decay time
$R_1 = 0.6$ = Output coupler reflectance
$R_2 = 1.0$ = Spherical mirror reflectance

Crystal parameters are:

$\sigma_p = 5.5 \times 10^{-24}$ = Cross section for absorption at 532 nm (fig. 5)
$\sigma_f = \lambda$ dependent = Cross section for emission (eqn. 2)
$N_{00} = 5.0 \times 10^{25} \text{m}^{-3}$ = Number density of Titanium
$\tau_{21} = 3.2 \times 10^{-6}\text{s}$ = Transition lifetime from state S_2 to S_1
$l = 15 \times 10^{-3}\text{m}$ = Crystal length

Pump parameters are:

$I_p = I_{p\ max} \exp[-\frac{(t-t_p)^2}{t_w^2}]$
$I_{p\ max} = \frac{E_p}{1.77 t_w a_g}$ = Maximum pump intensity
E_p = varied = Pump energy
$t_p = 90\text{ns}$ = Time of maximum pump energy
$t_w = 0.6 \times 20\text{ns} = 0.6 \times \text{FWHM}$
$a_g = 13 \times 10^{-6}\text{m}^2$ = Pump area at crystal
$\nu_p = \frac{c}{\lambda_p} = \frac{3 \times 10^8}{532 \times 10^{-9}} = 5.64 \times 10^{14}$ Hz = Pump frequency

It should be noted that the gaussian profile of the pump pulse is an approximation to the actual green pump temporal profile observed on the oscilloscope. The time of maximum pump energy was chosen in order to ensure that the full rise of the pump could be observed. Using a larger value than this would not affect the results of the model.

By choosing appropriate scaling factors we can cast these equations in a dimensionless form. This is a useful way of studying the equations, particularly in computer programs, since it avoids overflows from numbers which get too large when inappropriate units are used.

$$\frac{dx}{dz} = \frac{I_p}{I_{p_0}}(x_{00} - x) - x(y + \frac{\tau_c}{\tau_{21}}) \tag{21}$$

$$\frac{dy}{dz} = x(y + \frac{1}{y_0}) - y \tag{22}$$

where

$$x = \frac{N_2}{x_0} \qquad x_0 = \frac{L}{lc\sigma_f\tau_c}$$

$$y = \frac{n}{y_0} \qquad y_0 = \frac{La_r}{c\sigma_f\tau_c}$$

$$z = \frac{t}{z_0} \qquad z_0 = \tau_c$$

$$x_{00} = \frac{N_{00}}{x_0} \qquad I_{p_0} = \frac{h\nu_p}{\sigma_p\tau_c}$$

This summarises the formulae and parameteres used in the model for the temporal behaviour of the Ti:Sapphire laser.

4.1.2 Method of solution

The coupled rate equations in the preceding section can by solved by one of various numerical iterative methods. The method used in this work was the 4th order Runge-Kutta method developed by Carl Runge and Wilhelm Kutta. From an initial value, the method generates four auxiliary quantities from which the new value is computed. The implementation of this method for the equations 21 and 22 is as follows [28]:

$$
\begin{aligned}
k_1 &= dz[dx(x,y)] \\
m_1 &= dz[dy(x,y)] \\
k_2 &= dz[dx(x+\tfrac{1}{2}k_1, y+\tfrac{1}{2}m_1)] \\
m_2 &= dz[dy(x+\tfrac{1}{2}k_1, y+\tfrac{1}{2}m_1)] \\
k_3 &= dz[dx(x+\tfrac{1}{2}k_2, y+\tfrac{1}{2}m_1)] \\
m_3 &= dz[dy(x+\tfrac{1}{2}k_2, y+\tfrac{1}{2}m_1)] \\
k_4 &= dz[dx(x+k_3, y+m_3)] \\
m_4 &= dz[dy(x+k_3, y+m_3)]
\end{aligned}
$$

$$
\begin{aligned}
x &= x + \tfrac{1}{6}(k_1 + 2k_2 + 2k_3 + k_4) \\
y &= y + \tfrac{1}{6}(m_1 + 2m_2 + 2m_3 + m_4)
\end{aligned}
$$

with initial values

$$
\begin{aligned}
x_0 &= 0 \\
y_0 &= 0
\end{aligned}
$$

At each iteration the present value of the pump intensity was calculated and used in the differential equations for x and y. The time step used in the calculations was 1.4 ns as this was the resolution per pixel of the data obtained from the oscilloscope-CCD camera combination. Selected results were checked with smaller steps in order to assure the stability of the solution. For each run of the model, values of lasing wavelength, the total green pump energy, total red output energy, output pulse length and delay time between the green and red peaks were recorded.

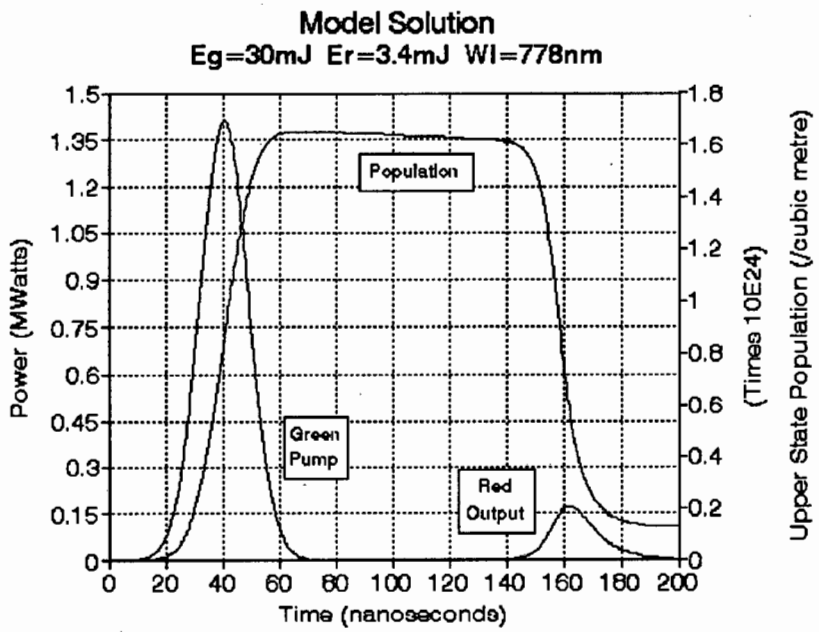

Figure 10: Example of Solution

Figure 10 shows an example of the solution of the coupled equations. The delay between the green input and the red output is clearly visible. The sudden onset of lasing is also apparent from the very abrupt drop in upper state population. Total pulse energies can be obtained by integrating the power over the duration of the pulse.

4.2 Spectral Model

The tuning prism determines the wavelength at which the Ti:Sapphire laser will lase. It also determines the width of the spectrum. The spread of wavelengths which are able to resonate in the dispersive cavity is limited by the requirement that the light must remain in the cavity after passing through the prism. Any ray which is capable of making a round trip in the cavity can contribute to the laser output. The range of wavelengths which satisfy this condition is termed the passive bandwidth [29]. This

bandwidth ($\Delta\lambda$) represents the maximum possible width of the output spectrum.

Since for lasing to occur at a particular wavelength a ray must pass repeatedly through a region of the crystal which has been pumped by the pump laser, the area of the pump at the crystal is a limiting factor on the bandwidth. The width of this region will be refered to as 'h'. This value was known and fixed for all data runs. An unknown factor which also affects the bandwidth is the divergence angle ('δ') of the fluorescence radiation. Various values of this parameter were tried in modelling runs.

The positions of all the elements of the laser must first be determined. This process follows exactly the physical procedure used to align the laser. The model then involves starting a ray of a particular wavelength off from the back face of the crystal with a particular displacement ($< h$) from the crystal axis and angle ($< \delta$) relative to this axis. The ray is then followed around the cavity, with every round trip being counted, until it either misses an element altogether or misses the active region of the crystal.

Chapter 5

Experimental and Model Results

5.1 Analysis of Data

All data was gathered in 30 shot runs at a 1 Hz repetition rate. Data was obtained for an initial set of tuned wavelengths of 742, 756, 778, 797 and 810 nm with a 50 mJ pump (1700 V). Four 30 shot runs were taken to give a total of 120 shots for each wavelength. Unfortunately the spectrometer was not sensitive enough at 810 nm to get reliable spectral data. This data showed that the pump laser was not working as reliably as possible. There were many shots which could not be used as the Nd:YAG either had not fired at all, or had produced a multimode output. It was therefore decided to change the saturable absorbing dye used to Q-switch the Nd:YAG. At 752 and 765 nm tuned wavelengths, sets of 120 shots for each of the pump energies 52, 45, 36 and 29 mJ (1700,1650,1600,1550 V) were taken. At the 765 nm wavelength this process was repeated for a vertically polarised pump as well.

A quick search of the images from the oscilloscope-CCD camera was first made in order to identify any dud shots (shots with either no pump or a multimode pump). These shots were then left out of all subsequent analysis. The oscilloscope images

were then "cleaned" in order to remove spurious jumps introduced by the software responsible for identifying the position of the trace which relies on the brightness of a particular pixel in the CCD array. This involved a simple smoothing process. The calibration image was then used to find the time represented by each pixel in the CCD array. Each CCD image was then analysed by identifying the position of the peaks of the green and red pulses. This gave the build up time in the Ti:Sapphire laser. The FWHM of the red pulse gave the pulse length of the ouput. Finally summing the intensity of the green pump, and red output gave a relative measure of the pump and output energies at a particular wavelength.

At a particular wavelength setting a computer program was used to calculate the wavelength corresponding to each pixel in the spectrometer array. The spectra were then analysed by fitting a parabola over the peak of each spectrum. The highest point in the spectrum was first found. A least squares fit of a parabola was then made to the points above half this height in order to get a simple "smoothing" of the spectrum. From this parabola the peak position and FWHM could be found.

5.2 Temporal Characteristics

5.2.1 Basic Model Results

Figures 11 and 12 show typical oscilloscope output with the corresponding model results superimposed. Note that the model pump peak occurs 16.8 ns before the experimentally observed one. This reflects the fact that the green light seen by the photodiode has been delayed by 16.8 ns during its passage through the optical fibre cable. The model intensities of the red and green pulses have been scaled in order to match those of the observed output. From these figures it is possible to begin making some conclusions about the accuracy of the model, but it is better to look at the summarised results of a large number of shots in order to see trends in the data.

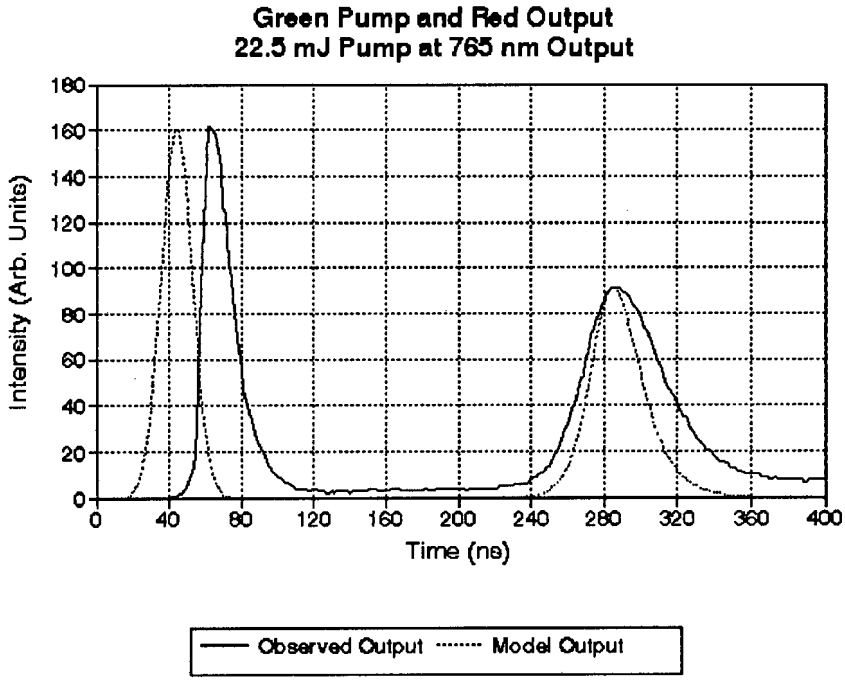

Figure 11: Example of Oscilloscope Data and Model

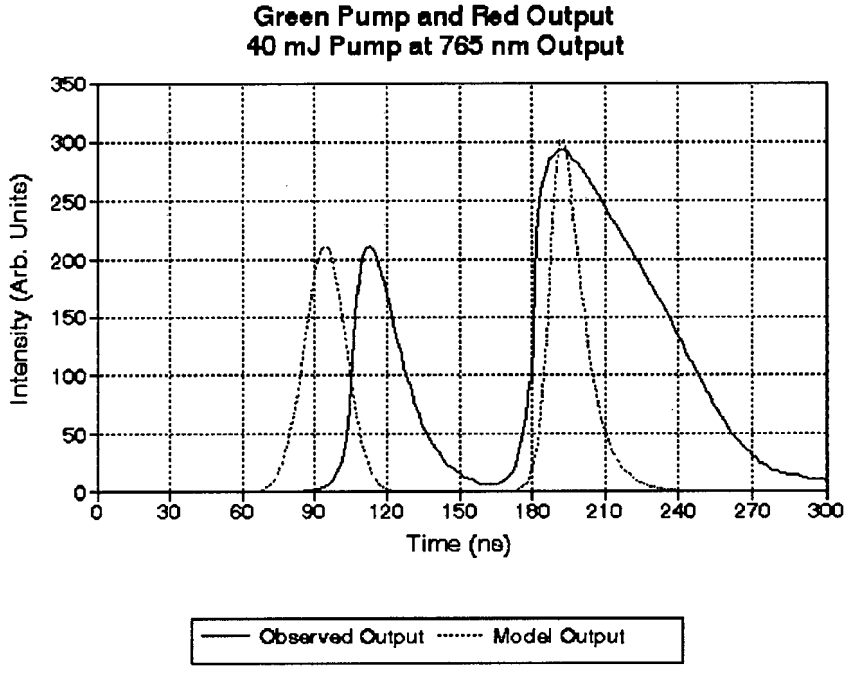

Figure 12: Example of Oscilloscope Data and Model

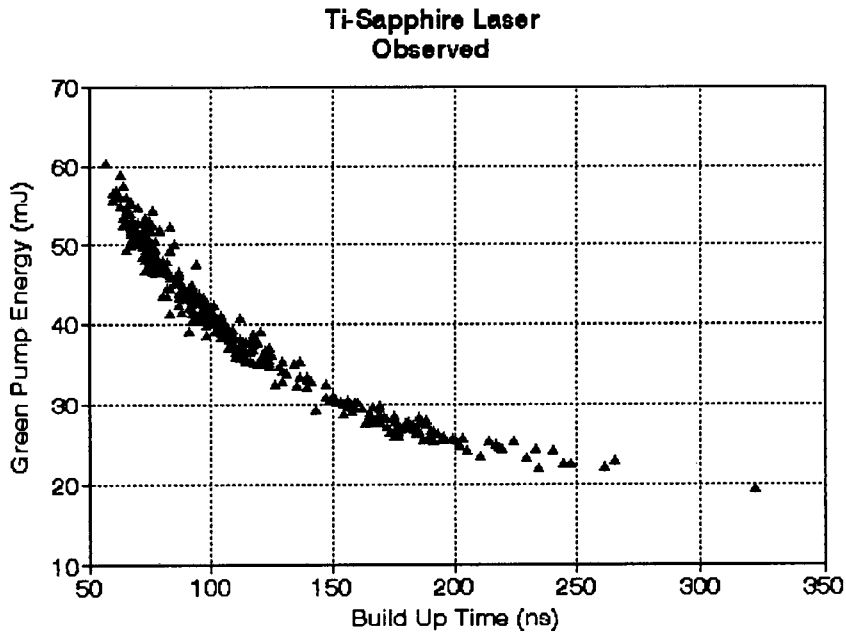

Figure 13: Observed Build Up Time at 765 nm

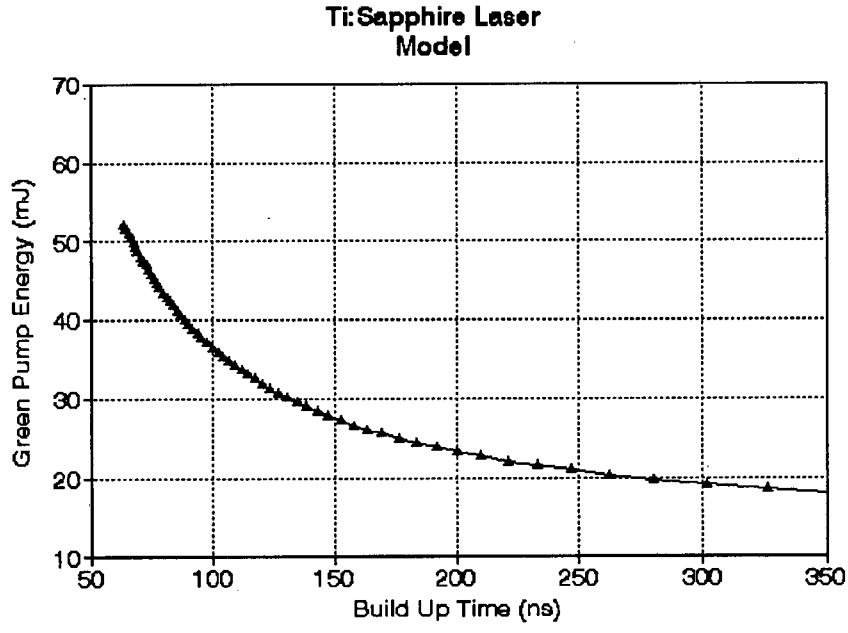

Figure 14: Model Build Up Time at 765 nm

Since for the final set of data at 765 nm the actual output energies could be calibrated, we will use this set for experimental-model comparisons. Figure 13 represents the results of the 411 good shots in that run. Figure 14 the corresponding model results with the same ranges and scales as those in the observed data. We note that the model fits the data very well, predicting both the general shape of the curve and the actual physical values.

Figures 15 and 16 show the relationship between red output energy and build up time. A striking feature of both sets of graphs involving the build up time is the almost "asymptotic" approach of the time towards a minimum value of 50 ns. Again the model fits the data well.

It is in figures 17 and 18 that we notice a significant difference between the model and the experimental results. The model predicts a continuous decrease in the pulse duration with decreasing build up time. For long build up the data follows this trend, however at a build up time of 170 ns, corresponding to a pump energy of 28 mJ and an output energy of 2.5 mJ, the pulse duration begins to turn around and lengthen again. Figure 11 shows the actual oscilloscope output in this region. The usual concave decay of the output intensity begins to become convex. This would suggest some sort of saturation effect which tends to cause the stored energy in the crystal to be released over a longer period than explained by the rate equations derived in the previous chapter. It is, however, difficult to identify the mechanism that might be causing this as no other characteristic output of the laser shows any deviation from the model at this same point. A run of the model with gain saturation included showed only a clamping of the pulse length at a maximum duration dependent upon the saturation intensity. No subsequent lengthening of the pulse was observed.

Finally the slope efficiency of conversion of pump energy into useful output is compared. The slope efficiency can be defined [22] by

$$E_{out} = \sigma_s(E_{in} - E_{threshold}) \tag{23}$$

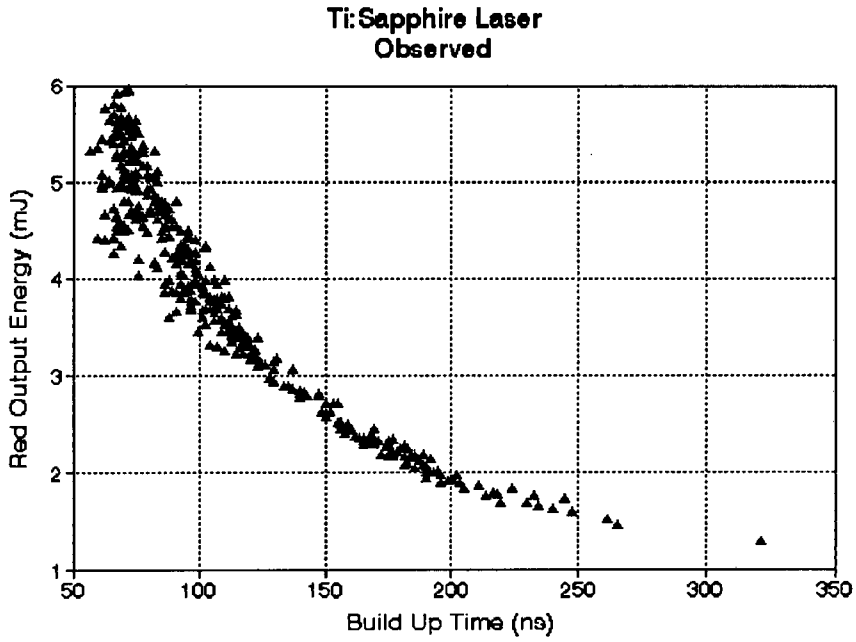

Figure 15: Observed Output Energies at 765 nm

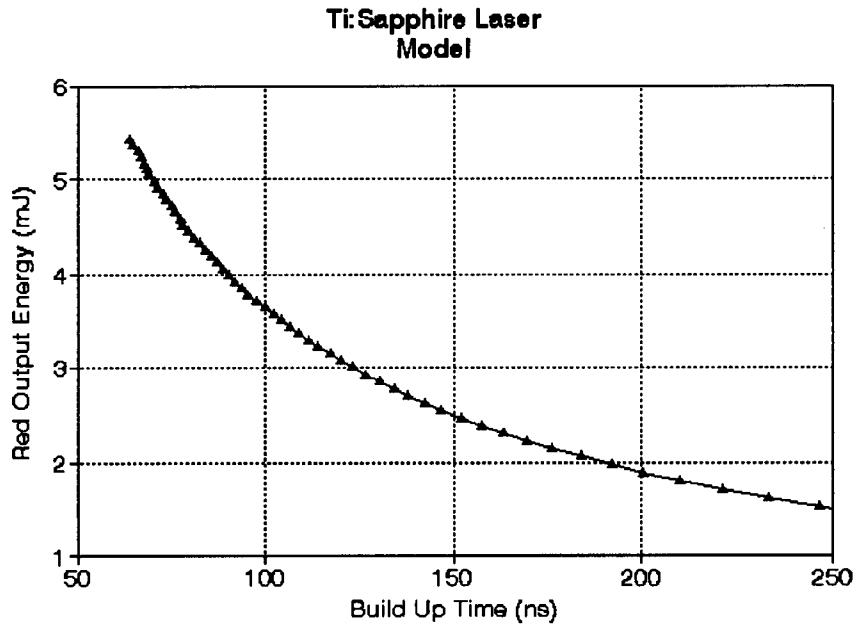

Figure 16: Model Output Energies at 765 nm

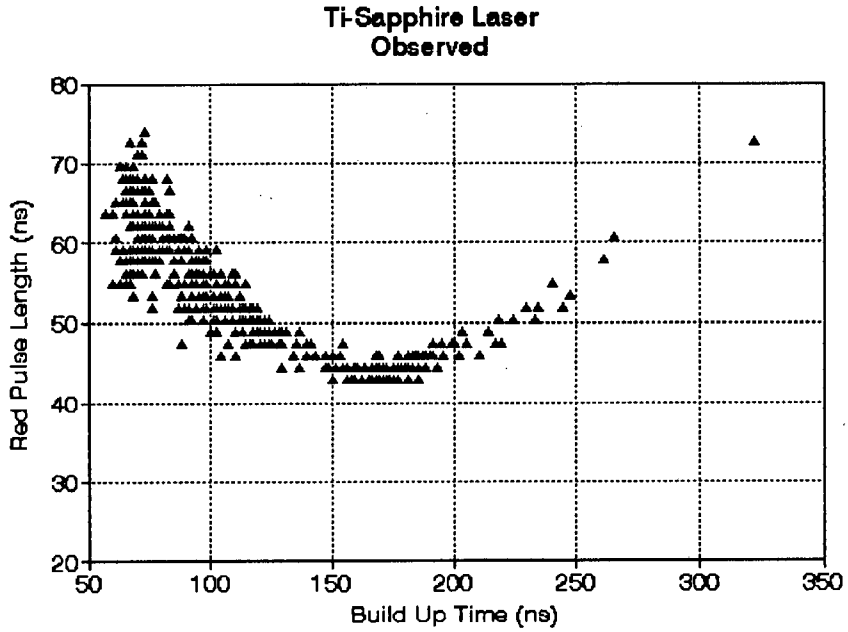

Figure 17: Observed Pulse Duration at 765 nm

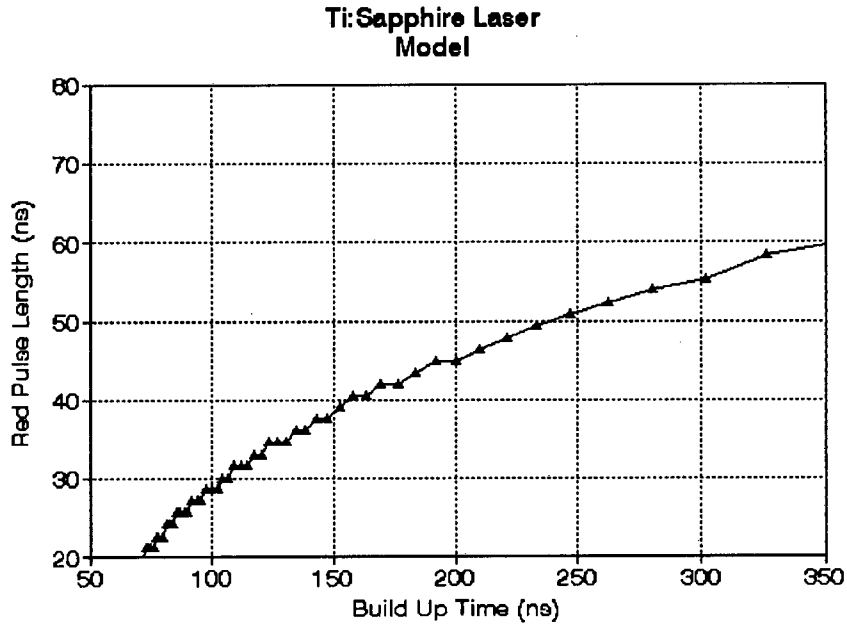

Figure 18: Model Pulse Duration at 765 nm

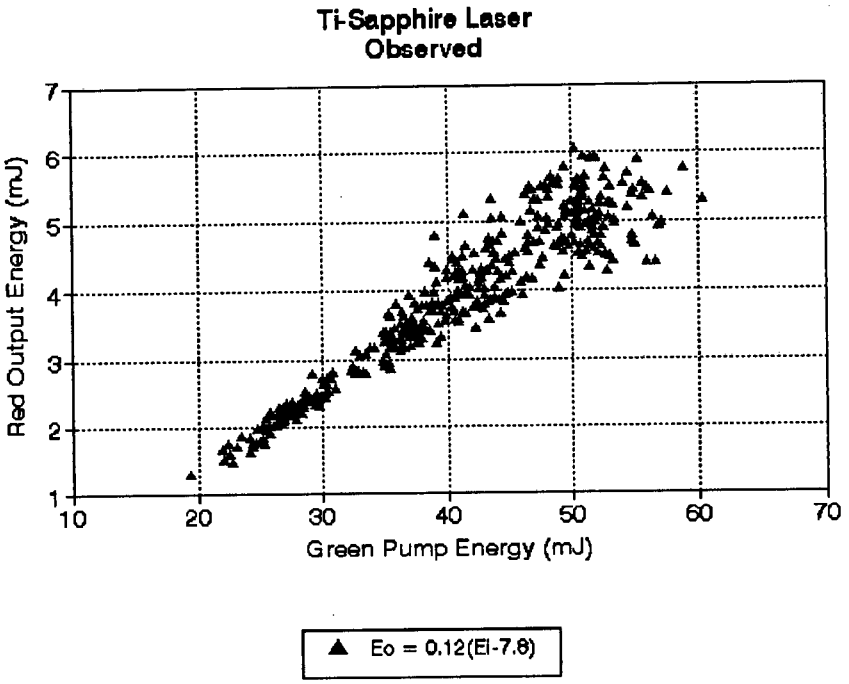

Figure 19: Observed Slope Efficiency at 765 nm

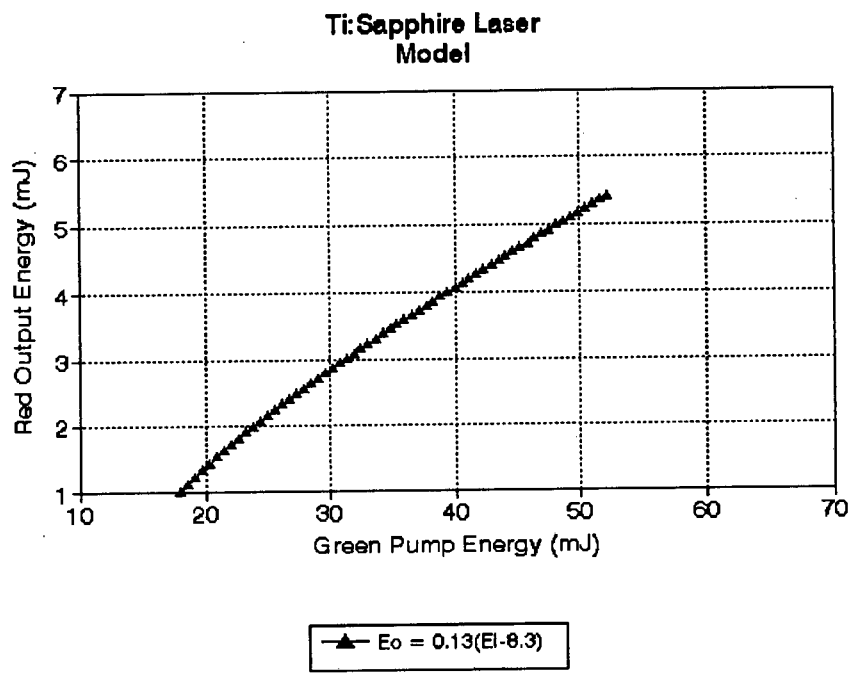

Figure 20: Model Slope Efficiency at 765 nm

where σ_s is the slope efficiency. The experimental data shows a value of 14% and the model gives 13% which represents an accuracy of within $\sim$ 10%. The data shows that although the energy spread for higher energy pumping is somewhat larger than for low energy pumping, the relationship is essentially linear.

5.2.2 Model Modified for Gain Saturation

Because the simple temporal model's predictions of the pulse length were not correct, the effect of gain saturation on the model output was investigated.

The unsaturated gain can be expressed as:

$$g(\nu) = \sigma_f(\nu) N_2 \tag{24}$$

where

$\sigma_f = \lambda$ dependent = Unsaturated cross section for emission
N_2 = Population of upper state

By including stimulated emission it can be shown that for homogeneously broadened emission ($Ti : Al_2O_3$ is predominantly thermally broadened), in a four level system, the saturated gain is given by [30]:

$$g_{sat}(\nu) = \frac{g(\nu)}{1 + \frac{E_r}{E_{sat}}} \tag{25}$$

where

E_r = Total energy of photons at wavelength ν contained in cavity
E_{sat} = Saturation energy

The saturation energy is then given by:

$$E_{sat} = \frac{h\nu a_r t_r}{\tau_{21}\sigma_f} \tag{26}$$

where

$h = 6.63 \times 10^{-34}$ Js = Planck's constant
$\tau_{21} = 3.2 \times 10^{-6}$ s = Transition lifetime from state S_2 to S_1
$a_r = 5 \times 10^{-7}\text{m}^2$ = Mode area
$t_r = 50$ ns = Average pulse duration

Now substituting equation 24 into 25 we see that an effective reduced fluorescence cross section can be obtained:

$$g_{sat}(\nu) = \frac{\sigma_f(\nu)}{1 + \frac{E_r}{E_{sat}}} N_2 = \sigma_{f(sat)} N_2 \tag{27}$$

Any term in the original model equations which contained a factor σ_f was thus divided by $(1 + \frac{E_r}{E_{sat}})$ in order to model the gain saturation. Equation 26 gives a value for the saturation energy of 0.073 mJ. In fact this value was found to be too low for the model and all red output effectively dissappeared. A value of 1.1 mJ was found to show the onset of saturation effects within the pump energy range observed. This value was therefore used in the model so that insight could be gained into the deviations from the more basic model.

Figure 21 shows the modified model output for a saturation energy of 1.1 mJ at a wavelength of 765 nm. Note that all these model graphs are plotted on the same axes as the graphs in the previous section for easy comparison. We can then note, when comparing figure 21 with figure 14, that the buildup time for a particular pump energy is essentially unchanged when saturation is included.

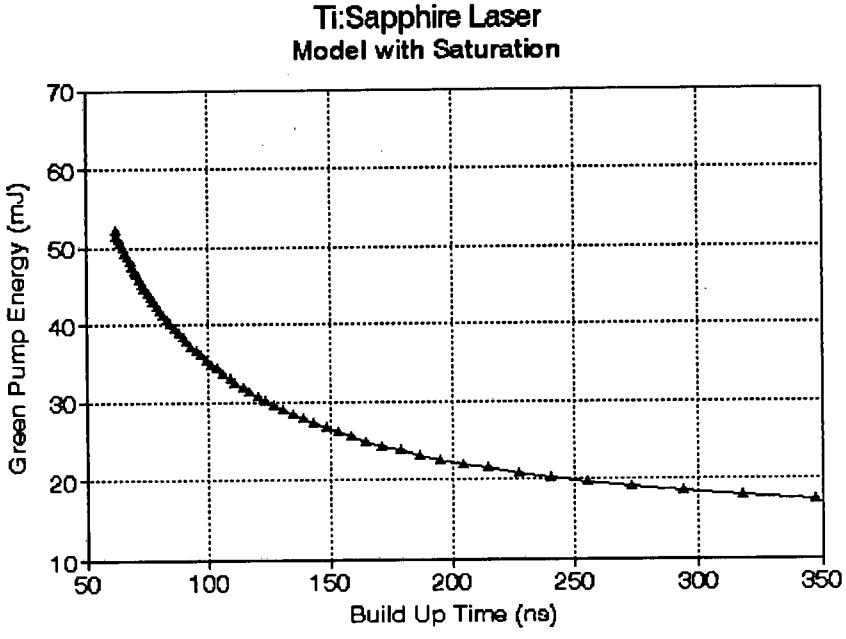

Figure 21: Model results at 765 nm with saturation

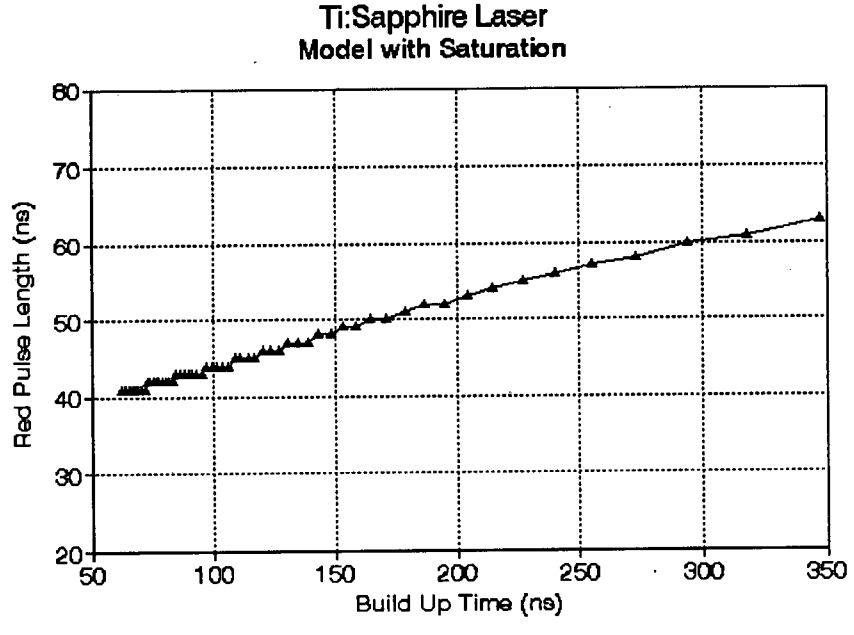

Figure 22: Model results at 765 nm with saturation

Figure 22 shows a noticable deviation from figure 18. The value of the saturation energy was chosen so that the modified model deviated from the basic one at approximately the same build up time as the observed data deviated from the basic model. We see that instead of a rapidly decreasing pulse duration with increasing pump, the modified model shows the pulse length leveling out and aproaching a constant value of 40 ns. This is a better fit to the data than the original model, however the observed output shows an increase in pulse length at high pump energies, a property still not fully explained by the gain saturated model.

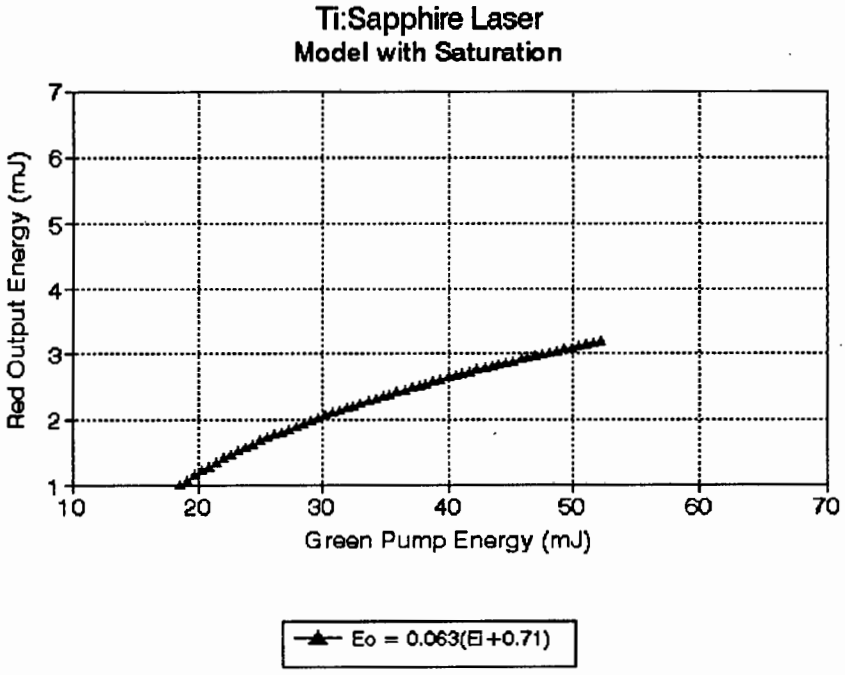

Figure 23: Model results at 765 nm with saturation

Finally figure 23 shows the slope efficiency obtained for the modified model. We see that a considerably lower output energy is predicted by the new model. The original model (figure 20) predicted the actual observed data far more accurately. Thus despite improving the prediction of the pulse length, the accurate prediction of the output energy has been lost. It therefore appears that there may well be saturation effects occuring, however the simple models presented here are not capable of describing these effects fully, though they go a surprisingly long way to predicting the laser's

operation with respect to build up time and energy conversions.

5.3 Spectral Characteristics

5.3.1 Wavelength Dependence of Spectral Width

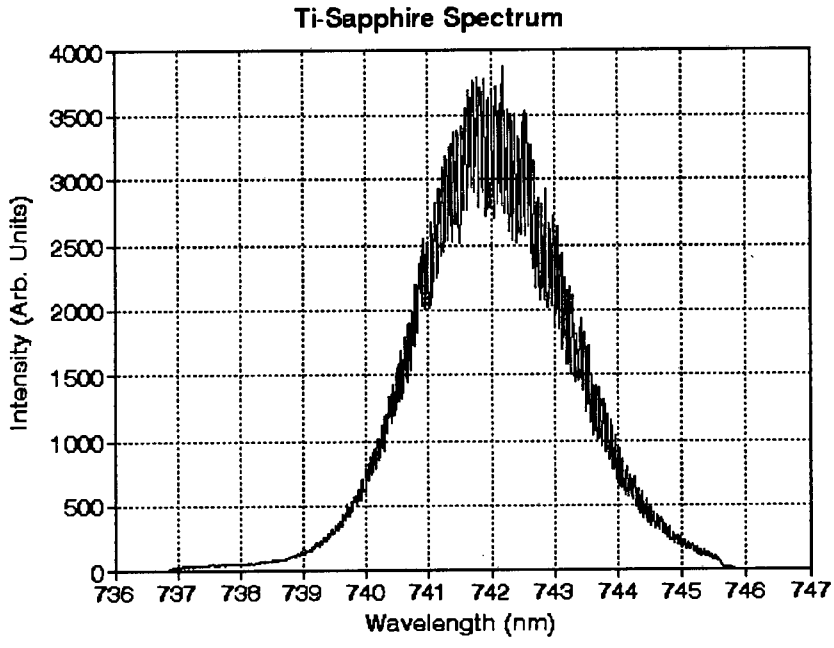

Figure 24: Observed Spectrum at 742 nm

Figures 24 and 25 show typical Ti:Sapphire laser output spectra. They are both averages of the 120 shots in a run. The broadening of the spectrum for longer tuned wavelengths is clearly apparent. Periodic structure in the profiles is also clear. This will be explored in more detail in a later section. For comparison figure 26 shows typical output from the model of the passive bandwidth. Since the position and orientation of the prism in the model was set so that the required central wavelength was exactly reflected back on itself, we can see that the central wavelength (distance from centre 0 nm), will make an infinite number of round trips without leaving the

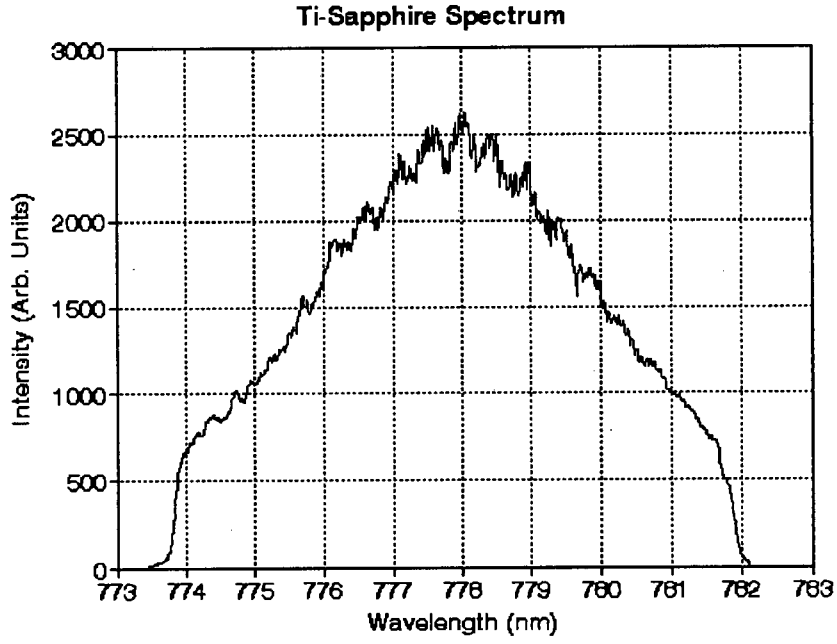

Figure 25: Observed Spectrum at 778 nm

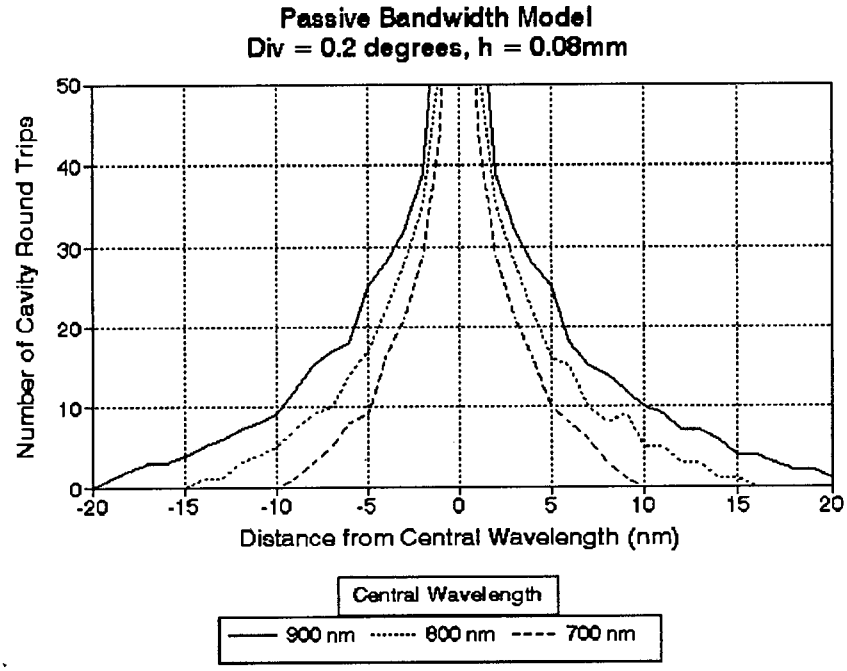

Figure 26: Model Spectrum Results

cavity. The increase in width of the spectral output for longer wavelengths is however shown, despite the fact that only the geometric optical characteristics of the cavity and no effects due to the variation in the emission cross section have been taken into account. The fine structure in the model is not physical and is presumably due to the size of the steps for the parameters δ and h.

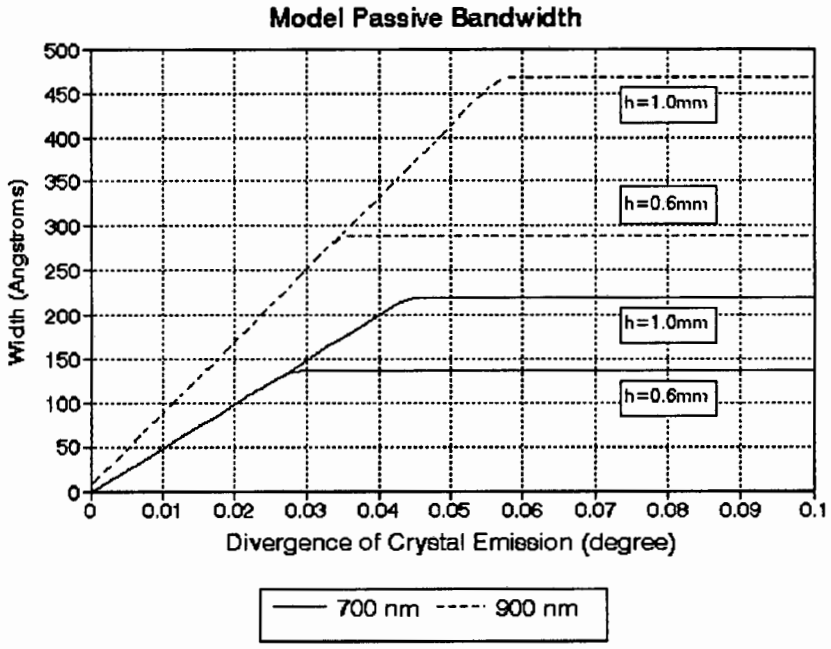

Figure 27: Passive Bandwidth Results

Figure 27 and figure 28 show the dependence of the passive bandwidth on various parameters. We can see in figure 27 that the height of the active region of the crystal only becomes significant for large divergence angles. Since our actual width data in figure 28 falls below the line with $\delta = 0.03$ degrees, the value of h does not actually limit the passive bandwidth as our laser appears to be working in the regime of δ limited bandwidth. Both figures also show the increase of passive bandwidth with increasing tuned wavelength. The data does, however, appear to climb more steeply than predicted by the model. This was to be expected, as this is a "passive" bandwidth. It represents the maximum possible bandwidth of the output, but at low wavelengths since we are far from the emission cross section peak at 800 nm, the

spectrum will not fill the passive bandwidth as much as at larger wavelengths where more modes, unfavoured by the dispersion effect of the prism, are still able to rise above threshold.

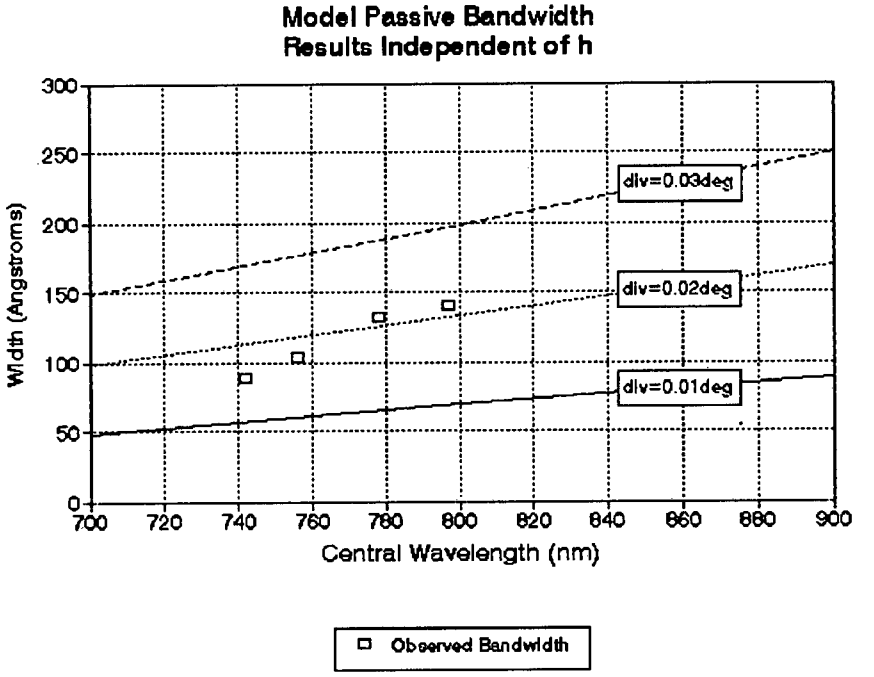

Figure 28: Passive Bandwidth Results

5.3.2 Energy Dependence of Spectral Output

An aspect of the operation of the Ti:Sapphire laser found to be fundamentally important in spectral noise was the energy dependence of the peak position and FWHM of the spectra.

Figure 29 clearly illustrates the effect. Each of the two spectra shown is an average of 120 shots at the same λ setting. It can be clearly seen that the spectrum broadens and moves to lower wavelengths with increasing pump power.

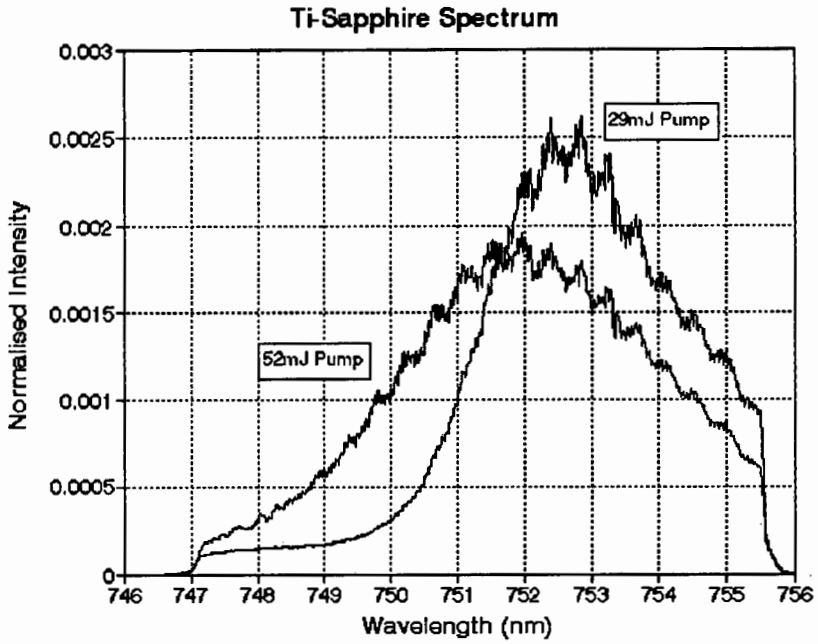

Figure 29: Averaged Spectra with Energy Dependence

A more quantitative measure of this property can be obtained by considering individual shots. The run at 765 nm was used for this as data was gathered for both horizontal (π) and vertical (σ) polarised pumps, ranging from an energy of 29 mJ to 52 mJ. The plots represent 411 good shots for the π pump and 336 for the σ pump.

Figure 30 shows an essentially linear relationship between the FWHM and output energy. We note also that the different polarisations fall on the same line. This is not surprising since the actual laser ouput was horizontally polarised in each case, so that essentially the only difference between the runs was the percentage of the pump absorbed.

Figure 31 shows the observed shift in peak position. Again a general linear trend is observed. There is, however, a splitting of the data; particularly obvious at the long wavelength end of the plot. This is most likely due to the periodic structure present in the spectrum profile (see fig. 25 for example). Because many shots had to be

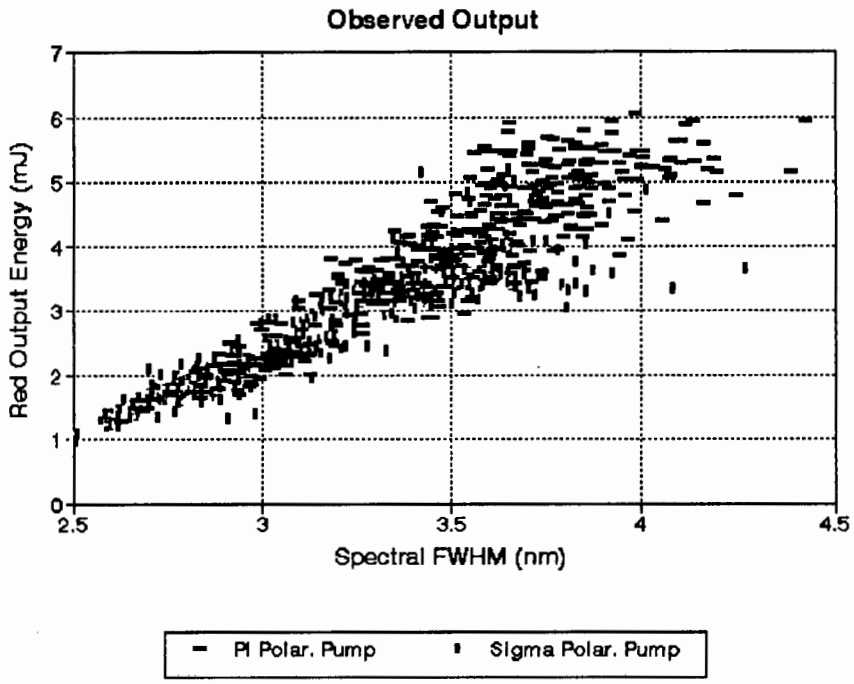

Figure 30: Energy Dependence of FWHM

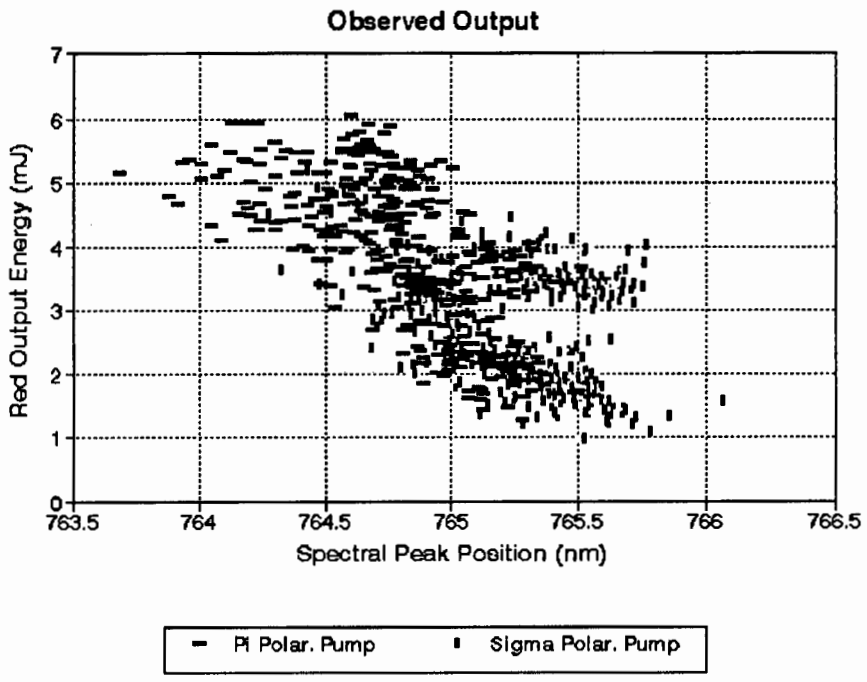

Figure 31: Energy Dependence of Peak Position

analysed, the fitting process was not as accurate as may have been desired. This may have resulted in the fitted peak being pulled towards a particularly prominent spike in the spectrum. The periodic structure created just such spikes, with particularly high points just to the left and just to the right of the actual spectrum peak. The fitted peak may thus have jumped between the left and right side depending upon which spike was higher in that particular spectrum.

5.3.3 Periodic Structure

As noted in the previous section, periodic structure was observed in the spectral output. This structure is larger than the separation between longitudinal cavity modes which is calculated to be of the order of 5×10^{-4} nm, considerably lower than the 1×10^{-2} nm resolution of the spectrometer.

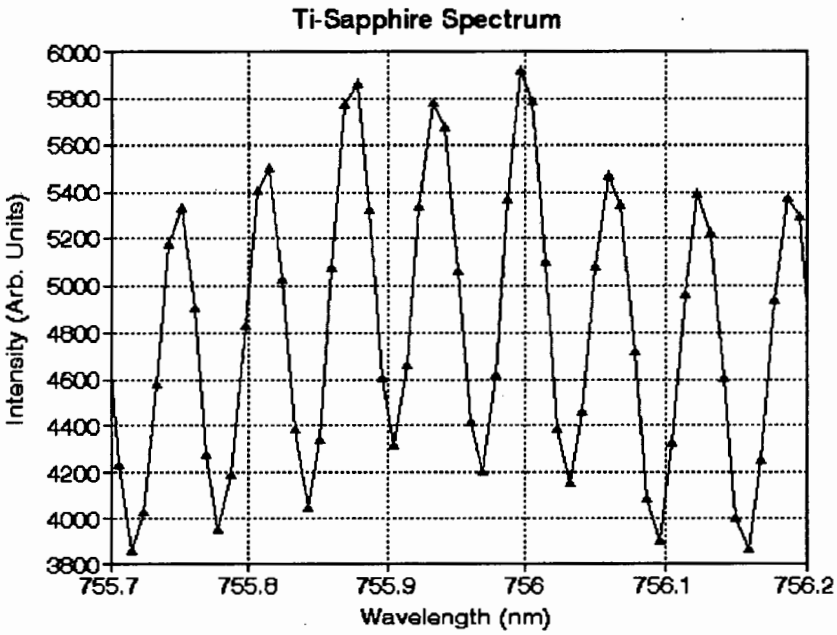

Figure 32: Enlarged Portion of Output Spectrum

Figure 32 shows an enlargement of the average spectrum for the run at 756 nm. The

fact that the structure survives the averaging process shows that it is an interference effect somewhere along the path of the light between the laser and the spectrometer which enhances certain wavelengths and suppresses others (the effect was not observed in spectra from the Tungsten filament used to determine the spectrometer response, so the possibilty of a spurious detector effect could be eliminated).

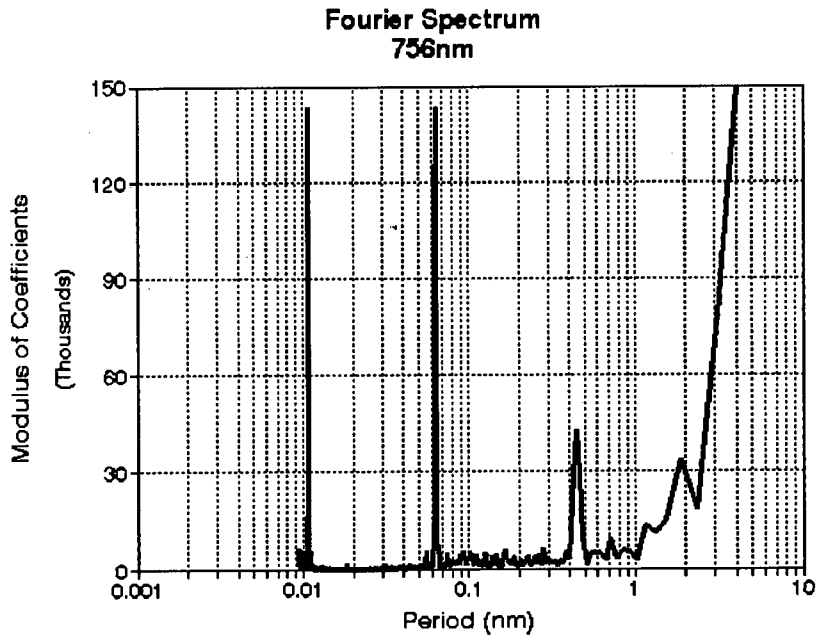

Figure 33: Determination of Fabry-Perot Cavity Length

Figure 33 is a Fourier Transform of the averaged spectrum for the 756 nm run. This process was also performed for the other spectra at different wavelengths. From the figure we can see three clear spikes at values of $\Delta\lambda$ of 0.011, 0.063, 0.44 nm. These same spikes were observed in spectra at other wavelengths with varying intensities. Using the criterion for constructive interference in a Fabry-Perot resonant cavity:

$$\nu_1 - \nu_2 = \frac{c}{2L} \qquad \Delta\lambda = \frac{\lambda_m^2}{2L} \tag{28}$$

where

c = Speed of light
$\nu_1 - \nu_2$ = Frequency spacing of resonances
L = Cavity length
$\Delta\lambda$ = Wavelength spacing of resonances
λ_m = Central Wavelength

From equation 28 the values of $\Delta\lambda$ can be used to calculate L. Three main cavity lengths were found: 26, 4.6 and 0.71 mm. It is not easy to identify the specific component causing this effect. It is expected to lie within the resonator cavity, since the light passes repeatedly around the cavity and would thus have an opportunity to interfere. The most likely candidate for the two smaller values is the output coupler, as it has a thickness of 5 mm and reflective coatings on the surfaces. Variations in the coating reflectivity may account for the fact that at different wavelengths one of the cavity lengths would produce a more noticeable effect than others. The source of the largest cavity could not be identified.

Chapter 6

Spectrum Noise

6.1 Method of Percentage Noise

A commonly used method for assessing the relative noise of different spectra is that of the percentage noise. Two possible methods were discussed by J.Horrel [31] in connection with the dye laser which is presently used for CARS spectroscopy in our laboratory. The two methods produce consistent results, but computational procedures are slightly different. In this work it was decided to use the method suggested by Snelling et al. [32][33] and Greenhalgh et al. [16], as it gives a noise value for each separate shot, which is then averaged in order to get an overall noise value for the run. This allows shot by shot investigation into the most important factors contributing to the noise values.

A set of spectra recorded by the OMA are represented by $C_i^{(k)}$ with

i = 1...P (Pixel Number)
k = 1...S (Shot Number)

These spectra can then be normalised in order to remove shot-to-shot energy variations which, as has been noted, are not important for CARS spectroscopy.

$$N_i^{(k)} \equiv \frac{C_i^{(k)}}{\sum_{i=1}^{P} C_i^{(k)}} \tag{29}$$

The normalised spectra are then averaged over all shots in order to obtain an average normalised spectrum against which the others may be compared.

$$\overline{N_i} = \frac{\sum_{k=1}^{S} N_i^{(k)}}{S} \tag{30}$$

Ratio'd spectra are then produced which eliminates any bias towards the peak of the spectrum.

$$R_i^{(k)} \equiv \frac{N_i^{(k)}}{\overline{N_i}} \tag{31}$$

An average ratio'd spectrum is then computed against which all spectra can be compared.

$$\overline{R^{(k)}} = \frac{\sum_{i=1}^{P} R_i^{(k)}}{P} \tag{32}$$

The standard deviation of each pixel of a spectrum from the average for that pixel is now determined.

$$\sigma^{(k)} = \left[\frac{\sum_{i=1}^{P} \left(R_i^{(k)} - \overline{R^{(k)}}\right)^2}{P}\right]^{\frac{1}{2}} \tag{33}$$

The noise value for each spectrum is now defined by

$$\gamma^{(k)} \equiv \frac{\sigma^{(k)}}{\overline{R^{(k)}}} \tag{34}$$

This can now be averaged for the whole run of shots in order to give the percentage noise.

$$\overline{\gamma} = \frac{\sum_{k=1}^{S} \gamma^{(k)}}{S} \tag{35}$$

6.2 Results

The noise analysis was performed with both 100 pixels and 200 pixels from each end of the array discarded in order to establish the effect of reducing the analysis bandwidth. This ensures that no edge effects in the detector sensitivity are included in the spectrum noise. Each noise value represents the result of a run of 120 shots. At high pump energies the Nd:YAG tended to produce multimode ouput. These shots could be identified from the oscilloscope output and removed from the analysis. Table 1 shows the results for the initial four runs before the Nd:YAG saturable absorber was changed. Table 2 represents the results with improved Nd:YAG performance. For comparison, table 3 shows selected dye laser results obtained by Horrell [31].

First of all we note that the noise taken with a 200 pixel edge is lower than that with 100 edge. This shows that the method is indeed dependent upon the analysis bandwidth and any comparisons must be made with this taken into account. The trends in the data are, however, the same for both edge values.

In table 1 we see that the noise value is reduced with increasing tuned wavelength. This is to be expected, since the peak of the emission cross section for $Ti : Al_2O_3$ occurs at 800 nm (see figure 2), so the closer the tuned wavelength gets to this the further the Ti:Sapphire laser is above threshold and it thus operates with more

stability. It is likely that the noise at 812 nm (the wavelength required for CARS, but not accessible with our detection system) will be similar to that at 797 nm .

Wavelength (nm)	Pump Energy (mJ)	Shots	Edge (pixels)	Noise%
742	52	84	100(200)	29.1(26.0)
756	52	105	100(200)	32.0(29.0)
778	52	111	100(200)	18.4(17.4)
797	52	120	100(200)	14.3(12.4)

Table 1: Wavelength dependence of Percentage Noise

Wavelength (nm)	Pump Energy (mJ)	Shots	Edge (pixels)	Noise%
752	52	90	100(200)	15.0(13.0)
752	45	80	100(200)	11.3(10.5)
752	36	98	100(200)	18.4(17.4)
752	29	94	100(200)	16.4(15.5)
765	52	85	100(200)	12.8(11.4)
765	45	89	100(200)	11.8(10.8)
765	36	117	100(200)	14.7(13.5)
765	29	120	100(200)	14.2(13.2)

Table 2: Energy dependence of Percentage Noise

Description of Dye	Edge (pixels)	Noise%
Rh610/Rh640 (oscillator only)	100	20.1
Rh610/Rh640 ($\frac{1}{3}$ concentration)	100	22.5
Rh610/Rh640 (tuned to 607 nm)	100	20.9
Rh610/SfRh101 (oscillator only)	100	18.6
Rh610/SfRh101 ($\frac{1}{3}$ concentration)	100	13.3
Rh610/SfRh101 (tuned to 607 nm)	100	15.4

Table 3: Dye laser Percentage Noise

This argument holds for table 2 as well. With a low energy pump the Ti:Sapphire laser is near threshold and thus not as stable as at higher pump energies. It is, however, interesting to note that at both wavelengths the maximum pump energy does not lead to the lowest noise figure. This may be due to instability in the Nd:YAG when it is run at high voltage. As noted previously the pump tends to operate multimode at these energies and it is thus reasonable to infer that there may also be a large

variation in the actual energy output at these voltages. This will be explored in more detail in the next section.

The results show that before the saturable absorber was replaced (table 1), the noise figures for the $Ti : Al_2O_3$ were in fact worse than those for the dye laser (table 3). Most notably, far from the $Ti : Al_2O_3$ gain peak (i.e. for smaller wavelengths), the noise figures for $Ti : Al_2O_3$ are worse than the worst figures obtained with the dye laser. A distinctly different situation occurs, however, after the saturable absorber had been renewed (table 2). Here the noise figures for the $Ti : Al_2O_3$ are better than the best observed dye combination. This confirms the idea that improved stability of the Nd:YAG pump pulse leads to a more stable and less noisy $Ti : Al_2O_3$ output.

6.3 Origins of Ti:Sapphire Noise

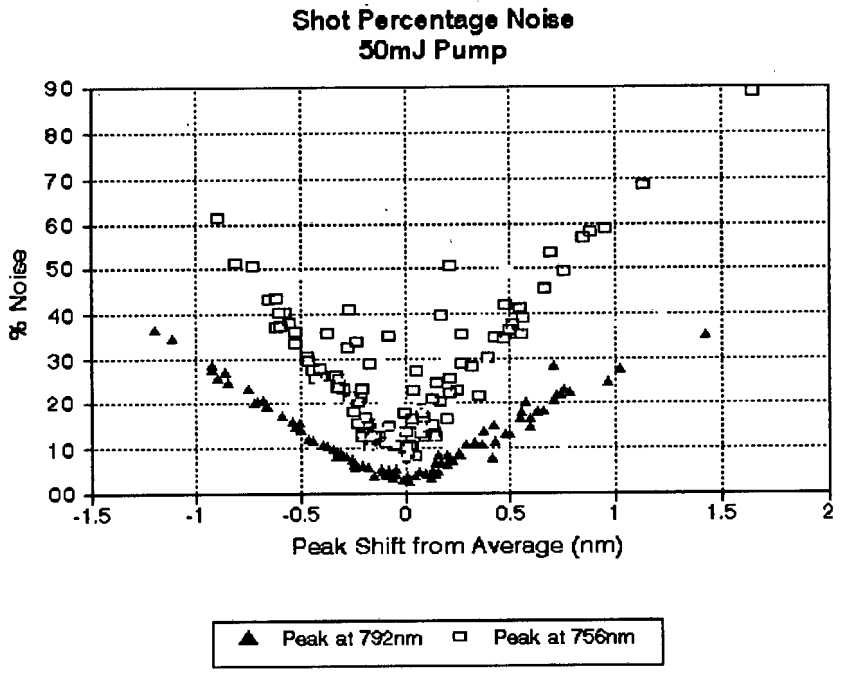

Figure 34: Noise values for specific shots

Figure 34 shows the contribution to the noise arising from each shot in a run. We can see that the shots with the highest noise values are those in which the peak of the spectrum has shifted furthest from the average peak position. This implies that the noise in the Ti:Sapphire laser is related to the shifting of the peak. It is also interesting to note that this effect is more pronounced when the laser is tuned to wavelengths far from the peak of the emission cross section at 800 nm. This arises because the FWHM for these spectra is smaller than that of longer wavelengths, thus creating a heightened sensitivity to shifts in the peak. In order to illustrate this we can compare figures 35 and 36.

The percentage noise is essentially a measure of the area between the averaged spectrum (original spectrum) and the shifted spectrum. Comparing the figures we can see that the same shift in peak position leads to a larger area between the curves in a spectrum with small FWHM if the bandwidth over which the noise is measured is kept constant. This offers another reason, over and above that of increased gain, for expecting the noise figures to be reduced for larger tuned wavelengths.

Figure 31 shows the reason for these shifts in peak position. Increases in pump energy lead to a shift in peak position towards shorter wavelengths. Careful observation of the Nd:YAG output shows a "warming up" period over which the energy of successive shots increases (figure 37). This variation in the actual green pump energy at a particular voltage setting leads to the shifting of the spectral peak and increased noise, in addition it will lead to changes in build up time (see figure 13) of the Ti:Sapphire laser which will also make CARS work difficult.

Thus realising in figure 34 that with a stable pump source one would avoid large peak shifts and all shots would lie at the bottom of the "bowl" formed by the rather unstable pump energies available to us, we can conclude that very low average noise values could be obtained. The minimum noise values for a run also decrease as one approaches the wavelength corresponding to the peak of the gain curve ($\sim$ 800 nm). With the Ti:Sapphire laser tuned to 812 nm and using a very stable pump source we can conclude that noise values below 10% could readily be achieved.

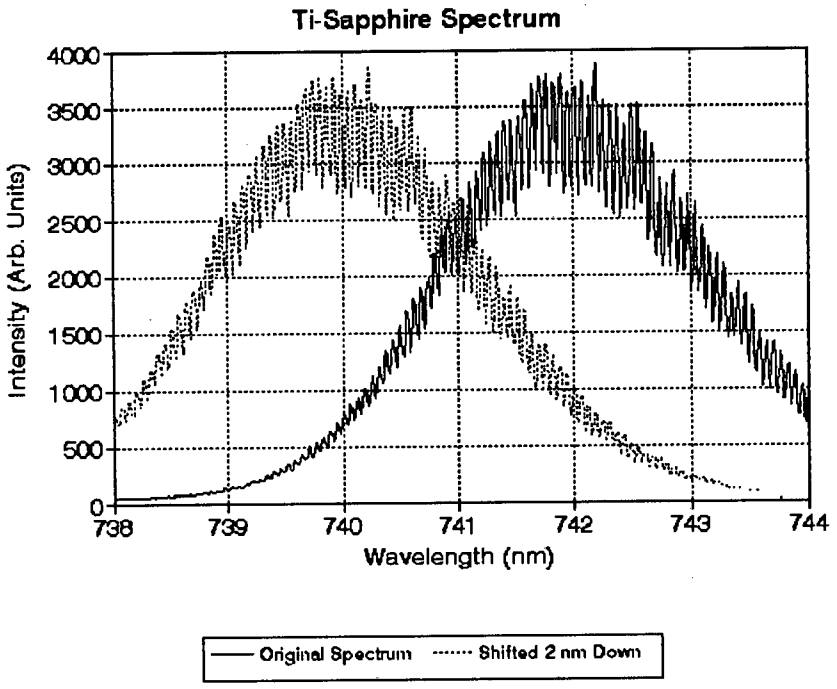

Figure 35: Effect of Shifted Shot at 742 nm

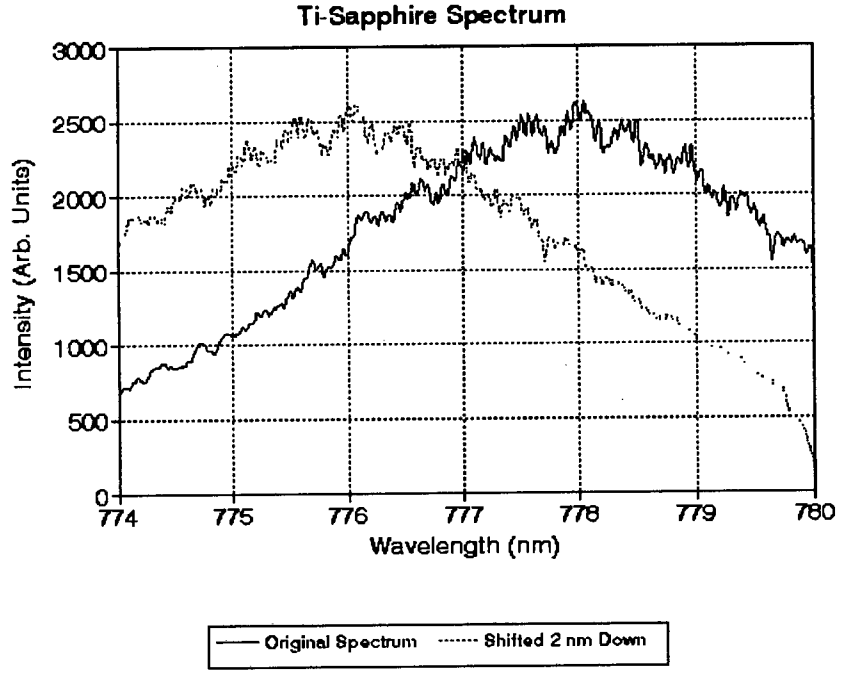

Figure 36: Effect of Shifted Shot at 778 nm

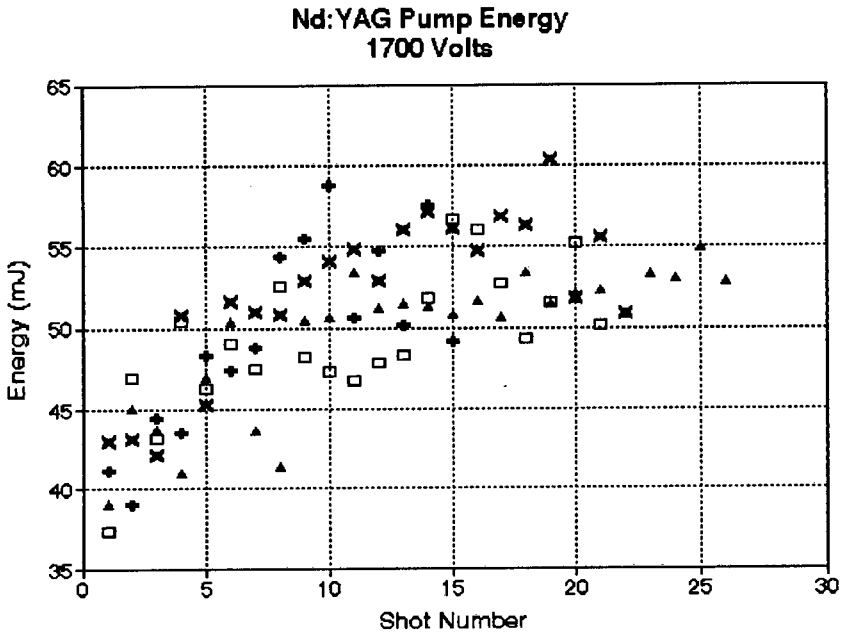

Figure 37: Pump Energy Variations

Chapter 7

Conclusions

7.1 Results and Modelling

All the relevant modelling parameters could be obtained either by direct measurement or the literature. This enabled us to construct a simple coupled rate equation model of the operation of the Ti:Sapphire laser. Effective computer programmes allowed us to gather and analyse large sets of data so that important trends could be recognised. The temporal model gave a very good fit to all characteristics of the laser operation except the pulse length. The reduction of $Ti : Al_2O_3$ build up time with increasing pump energy was clearly illustrated. The slope efficiency of 12% at 765 nm was also well predicted. The results showed that the Ti:Sapphire laser is actually stable in the sense that for a particular pump energy the build up time can be accurately predicted. Unfortunately, however, simply setting the Nd:YAG at a particular voltage does not allow one to predict the shot-by-shot build up as random variation in the pump affects the Ti:Sapphire laser output.

An attempt was made to explain the anomalous lengthening of the duration of the red output for high pump energies. The effects of saturation could clearly be seen

in the model results, in that the pulse length approached a constant time for high pump energies, however they did not fully explain the turnaround in the observed data. More sophisticated modelling, taking into account the mode competition in the $Ti : Al_2O_3$ laser may be necessary, but is beyond the scope of the present investigation.

The model of the spectral output was able to predict the broadening of the spectrum for longer wavelengths purely through geometrical optics considerations. It is likely, however, that power broadening also becomes more important as one approaches wavelengths near the fluorescence peak. This appears to be borne out by the observations of the FWHM at 765 nm where a clear broadening is observed for increasing output energies.

7.2 Viability of CARS

A few of the important factors required of a Stokes beam for successful CARS will now be discussed with reference to the observed operation of the Ti:Sapphire laser.

Firstly it is important to be able to tune the Stokes beam wavelength accurately in order to ensure the energy difference between pump and Stokes is the required wavelength. This tuning process was found to be very easy, as the red ouput could be watched on the spectrometer as the prism was slowly turned. This allowed immediate changes to be made. If the correct wavelength was not obtained the prism could simply be turned slightly. With practice these adjustments became more and more accurate.

The pump and Stokes beams have to mix in the chamber where CARS measurements are to be made. We have seen that the Ti:Sapphire laser takes a finite time to build up to above threshold. The pump beam thus has to be made to travel a path long enough that when the Ti:Sapphire laser output emerges, the pump is ready to meet it. An accurate knowledge of the exact build up time is therefore required. It has already

been observed that the stability of the Nd:YAG pump is crucial to the shot-to-shot predictability of the build up time. There is, however, a further requirement that the distance the pump beam has to travel in the meantime is in fact practically possible inside the laboratory. The longest delay time (320 ns) observed represents a delay distance of 96 m which would not really be viable for CARS work. The shortest (60 ns) represents a distance of 18 m which would be more practicable for CARS work, however it also takes all the maximum green pump energy. A green pump energy of 35 mJ would produce a delay of some 30 m, which with careful mirror alignment could be achieved, while still leaving Nd:YAG pump over to be used to produce the CARS pump beam.

Sufficient energy is required in the Stokes beam in order to initiate the CARS interaction. This would not seem to be a problem since only 2 or 3 mJ would be required. These output energies were achieved for pump energies of between 25 and 30 mJ at a tuned wavelength of 765 nm. It was observed that the Ti:Sapphire laser works more efficiently at wavelengths near the fluorescence peak, so one could expect the red yield to be even higher at the 812 nm required for CARS.

Finally the spectral profile should be stable from shot to shot. It was shown that after the stability of the Nd:YAG was improved by renewing the saturable absorber the noise values were drastically reduced. Further investigation showed that the biggest contributors to the average noise over a run of shots were those shots whose peaks moved furthest from the average. Stabilising the position of the Ti:Sapphire laser spectral peak is therefore of the utmost importance. Since there was a distinct relationship between the pump energy and the peak position, further efforts to stabilise the Nd:YAG laser may well lead to even better noise figures. Under optimum conditions the Ti:Sapphire laser showed less noise than the dye laser previously used in our laboratory, so the hypothesis that a solid state laser would produce a more stable spectrum would appear to be justified in this case.

Bibliography

[1] L.Johnson R.Dietz H.Guggenheim. Optical maser oscillation from Ni^{2+} in MgF_2 involving simultaneous emission of photons. *Physical Review Letters*, 11:318–320, 1963.

[2] J.Walling H.Jensen R.Morris E.O'Dell O.Peterson. Tunable alexandrite lasers. *IEEE J. Quantum Electron*, 16:1302–1315, 1980.

[3] P.F.Moulton. Spectroscopic and laser characteristics of $Ti : Al_2O_3$. *J. Opt. Soc. Am. B*, 3:125–132, 1986.

[4] A.Sanchez R.Fahey A.Strauss R.Aggarwal. Room-temperature continuous-wave operation of a $Ti : Al_2O_3$ laser. *Optics Letters*, 11:363, 1986.

[5] N.P.Barnes J.Williams J.C.Barnes G.Lockard. A self-injection locked, Q-switched, line narrowed $Ti : Al_2O_3$ laser. *IEEE J. Quantum Electronics*, 24:1021–1028, 1988.

[6] P.Schultz. Single-frequency $Ti : Al_2O_3$ ring laser. *IEEE J. Quantum Electron*, 24:1039, 1988.

[7] C.Muller D.Lowenthal K.Kangas R.Hamil G.Tisone. 2.0-J Ti:Sapphire laser oscillator. *Optics Letters*, 13:380, 1988.

[8] P.Albers E.Stark G.Huber. Continuous-wave laser operation and quantum efficiency of titanium-doped sapphire. *J. Optical Society of America B*, 3:134–139, 1986.

[9] J.Eggleston L.DeShazer K.Kangas. Characteristics and kinetics of laser-pumped Ti:Sapphire oscillators. *IEEE J. Quantum Electron*, 24:1009–1015, 1988.

[10] D.Snelling T.Parameswaran G.Smallwood. Noise characteristics of single-shot broadband cars signals. *Applied Optics*, 26:4298–4302, 1987.

[11] S.Kröll M.Aldén T.Berglind R.Hall. Noise characteristics of single shot broadband Raman-resonant CARS with single- and multimode lasers. *Applied Optics*, 26:1068–1073, 1987.

[12] R.Hall D.Greenhalgh. Noise properties of single-pulse coherent anti-Stokes Raman spectroscopy with multimode pump sources. *J. Optical Society of America B*, 3:1637–1641, 1986.

[13] M.Pealat P.Bouchardy M.Lefebvre J.-P. Taran. Precision of multiplex CARS temperature measurements. *Applied Optics*, 24:1012–1022, 1985.

[14] S.Curry R.Cubeddu T.Hänsch. Intensity stabilization of dye laser radiation by saturated amplification. *Applied Physics*, 1:153–159, 1973.

[15] L.Westling M.Raymer J.Snyder. Single-shot spectral measurements and mode correlations in a multimode pulsed dye laser. *J. Optical Society of America B*, 1:150–154, 1984.

[16] D.Greenhalgh S.Whittley. Mode noise in broadband CARS spectroscopy. *Applied Optics*, 24:907–913, 1985.

[17] D.Snelling R.Sawchuk T.Parameswaran. Noise in single-shot broadband coherent anti-Stokes Raman spectroscopy that employs a modeless dye laser. *Applied Optics*, 33:8295–8301, 1994.

[18] P.Snowdon S.Skippon P.Ewart. Improved precision of single-shot temperature measurements by broadband CARS by use of a modeless laser. *Applied Optics*, 30:1008–1010, 1991.

[19] G.Morrison. Backward Stimulated Raman Scattering. Master's thesis, University of Cape Town Physics Dept., 1993.

[20] R.Weast. *Handbook of Chemistry and Physics.* CRC Press, New York, 1974.

[21] F.Duarte L.Hillman. *Dye Laser Principles with Applications.* Academic Press Inc., San Diego, 1990.

[22] W.Koechner. *Solid-State Laser Engineering.* Springer-Verlag, Heidelberg Germany, 1992.

[23] R.Chiao E.Garmire C.Townes. Self trapping of optical beams. *Physical Review Letters*, 13:479–482, 1964.

[24] E.Dawes J.Marburger. Computer studies in self-focusing. *Physical Review*, 179:862–868, 1969.

[25] W.Wagner H.Haus J.Marburger. Large-scale self-trapping of optical beams in the paraxial ray approximation. *Physical Review*, 175:255–266, 1968.

[26] P.Kelley. Self-focusing of optical beams. *Physical Review Letters*, 15:1005–1008, 1965.

[27] W.Rapoport C.Khattak. Efficient, tunable Ti:Sapphire laser. *Conference on Tunable Solid-State Lasers*, 1988.

[28] P.Milonni J.Eberly. *Lasers.* Wiley, New York, 1988.

[29] C.Ottinger A.Slenczka V. Wulfmeyer. Development and theoretical modelling of a broadband, tunable, pulsed dye laser. *Applied Optics*, 33:935–943, 1994.

[30] O.Svelto. *Principles of Lasers.* Plenum, New York, 1989.

[31] J.Horrel. Investigation of broadband laser spectral fluctuations with application to CARS. Master's thesis, University of Cape Town Physics Dept., 1993.

[32] D.Snelling R.Sawchuk R.Mueller. Single pulse CARS noise: a comparison between single-mode and multimode pump lasers. *Applied Optics*, 24:2771–2778, 1985.

[33] D.Snelling G.Smallwood R.Sawchuck T.Parameswaran. Precision of multiplex CARS temperatures using both single-mode and multimode pump lasers. *Applied Optics*, 26:99–110, 1987.